



## OPEN Thermal cooling efficacy of a solar water pump using Oldroyd-B (aluminum alloy-titanium alloy/engine oil) hybrid nanofluid by applying new version for the model of Buongiorno

Faisal Shahzad<sup>1</sup>, Wasim Jamshed<sup>1</sup>, Mohamed R. Eid<sup>2,3✉</sup>, Rabia Safdar<sup>4</sup>, Siti Suzilliana Putri Mohamed Isa<sup>5</sup>, Sayed M. El Din<sup>6</sup>, Nor Ain Azeany Mohd Nasir<sup>7</sup> & Amjad Iqbal<sup>8,9</sup>

Solar radiation, which is emitted by the sun, is required to properly operate photovoltaic cells and solar water pumps (SWP). A parabolic trough surface collector (PTSC) installation model was created to investigate the efficacy of SWP. The thermal transfer performance in SWP is evaluated thru the presence of warmth radiation and heat cause besides viscid dissipation. This evaluation is performed by measuring the thermal transmission proportion of the selected warmth transmission liquid in the PTSC, known as a hybrid nano-fluid. Entropy analysis of Oldroyd-B hybrid nano-fluid via modified Buongiorno's model was also tested. The functions of regulating parameters are quantitatively observed by using the Keller-box approach in MATLAB coding. Short terms define various parameters for tables in velocity, shear pressure and temperature, gravity, and Nusselt numbers. In the condition of thermal radiation and thermal conductivity at room temperature, the competence of SWP is proven to be enhanced. Unlike basic nano-fluids, hybrid nano-fluids are an excellent source of heat transfer. Additionally, with at least 22.56% and 35.01% magnitude, the thermal efficiency of AA7075–Ti–6Al–4V/EO is higher than AA7075–EO.

### Abbreviations

$B_r$	Brinkman number
$Bi$	Biot number
$b$	Stretching rate
$C_p$	Specific heat ( $Jkg^{-1}K^{-1}$ )
$D_B$	Mass diffusion coefficient
$h_f$	Heat transfer coefficient
$h$	Concentration (dimensionless)

<sup>1</sup>Department of Mathematics, Capital University of Science and Technology (CUST), Islamabad 44000, Pakistan. <sup>2</sup>Department of Mathematics, Faculty of Science, New Valley University, Al-Kharga 72511, Al-Wadi Al-Gadid, Egypt. <sup>3</sup>Department of Mathematics, Faculty of Science, Northern Border University, Arar 1321, Saudi Arabia. <sup>4</sup>Department of Mathematics, Lahore College for Women University, Lahore 54000, Pakistan. <sup>5</sup>Institute for Mathematical Research, Universiti Putra Malaysia, UPM, 43400 Serdang, Seri Kembangan, Selangor Darul Ehsan, Malaysia. <sup>6</sup>Center of Research, Faculty of Engineering, Future University in Egypt, New Cairo 11835, Egypt. <sup>7</sup>Department of Mathematics, Centre for Defence Foundation Studies, Universiti Pertahanan Nasional Malaysia, Kem Sungai Besi, 57000 Kuala Lumpur, Malaysia. <sup>8</sup>Department of Materials Technologies, Faculty of Materials Engineering, Silesian University of Technology, 44-100 Gliwice, Poland. <sup>9</sup>CEMMPRE—Centre for Mechanical Engineering Materials and Processes, Department of Mechanical Engineering, University of Coimbra, Rua Luí's Reis Santos, 3030-788 Coimbra, Portugal. ✉email: m\_r\_eid@yahoo.com

$K$	Porous medium parameter
$N_r$	Radiation parameter
$N_G$	Entropy generation (dimensionless)
$Nu_x$	Local nusselt number
$Sh_x$	Local sherwood number
$q_r$	Radiative heat flux
$q_w$	Wall heat flux
$Re$	Reynolds number
$S$	SAuction/injection parameter
$v_1, v_2$	Velocity component ( $ms^{-1}$ )
$U_w$	Stretching velocity
$V_w$	Vertical velocity
$x, y$	Dimensional space coordinates ( $m$ )
$N_w$	Slip length
$\mu$	Dynamic viscosity ( $kgm^{-1}s^{-1}$ )
$\nu$	Kinematic viscosity ( $m^2s^{-1}$ )
$\alpha$	Chemical reaction parameter
$\omega$	Similarity variable
$\theta$	Temperature (dimensionless)
$\psi$	Stream function

### Subscripts

$f$	Base fluid
$p_1, p_2$	Nanoparticles
$nf$	Nano-fluid
$hnf$	Hybrid nano-fluid
$s$	Particles
AA7075	Aluminum alloy
Ti-6Al-4 V	Titanium alloy

### Greek symbols

$\Theta$	Dimensional temperature
$\Theta_w$	The dimensional temperature of the surface
$\Theta_\infty$	Ambient temperature
$\phi$	Solid volume fraction
$\rho$	Density ( $Kgm^{-3}$ )
$\sigma^*$	Stefan Boltzmann constant
$C^*$	Dimensional concentration

Solar energy, radiation from the sun, can generate heat, trigger chemical responses, or reproduce electricity. The world's quantity of solar energy is much superior to the contemporary and expected universal energy needs. Solar Photovoltaic (PV) and Solar Thermal<sup>1</sup> are two categories of solar energy technology. PV technology converts sunlight into electricity through photovoltaic semiconductors<sup>2</sup>, whereas Solar Thermal is a technology that directly uses solar energy to heat or generate electricity. Solar water heating systems are the technology from Solar Thermal that collect heat through the solar collector to heat water for domestic or commercial purposes<sup>3</sup>. Using non-renewable fossil fuels in the plantation is to boil water<sup>4</sup>, which can also be performed by solar thermal technology. Therefore, solar energy is needed to sustain the environment and population growth<sup>5</sup>. Solar energy usage can be observed in any PV technologies, such as streetlights, solar water propels, profitable power developments, net metering ventures, and solar construction technology<sup>6</sup>. While agricultural experts question the legitimacy of organic and local food security, grocery shops around the country have begun to stock organic and local food. Organic and locally sourced products are more popular among consumers, and the desire for these items has increased rapidly in recent years. The integration of the natural and local cuisine movements has resulted in a variety of marketing options, ranging from local cuisine units in major supermarkets to farmers' shops and community-based agriculture systems (CSA)<sup>7</sup>. PV technology, on the other hand, is one of the most common forms of solar systems accessible, and it includes a collection of PV solar panels referred to as solar cell systems<sup>8</sup>. CSP, or concentrated solar power, is commonly found in vast regions producing grid electricity. CSP solar water heating begins with black paint applied on the leg and is utilised to heat water. Because dark colours capture the heat of the sun, they heat the water within. Although this may appear archaic, it demonstrates that humankind knew the sun's energy from the outset. The heat produced by this mechanism is comparable to the quantity of heat produced by the sun. As a result, countries with scorching suns and tropical climates are more prone to profit from this form of solar energy. This advantage includes the efficacy of such initiatives. As a result, in hot climates, hydropower can be expensive. As a consequence, reimbursement times for solar eclipses are shorter<sup>9</sup>. Fluid runs through tubes and gathers solar energy in CSP to heat water or create electricity. One issue with this solar power is heat transmission from the sun. Scientists and innovators tried other liquids, such as oil and sodium, yet molten salt proved to be an exceptionally successful alternative. This alternative is good, considering it is more expensive and works better with steam engines. Compared to solar PV, solar power works much better in space. Solar thermal can provide up to 70% efficiency in heat collection<sup>10</sup>.

A solar water pump (SWP) system is an electric pump water system for electricity production, where one or more PV panels supply electricity. A standard SWP system consists of a solar panel that empowers an electric motor, which enables a shaft directly above the pump. H<sub>2</sub>O is usually pumped starting the ground or flowing into a storage reservoir that supplies gravitational force. Thus vitality conservation is not required in these systems<sup>11</sup>. The solar pressure regulator is driven by electricity supplied by the PV array or radiant heat created by solar light collected. This solar water pump works opposite to a diesel or grid compressor<sup>12</sup>. In 1983, the creator of the United States, Charles Fritts, documented the very first photovoltaic cells built using water pumps and live electricity in 15 residences. Until 1993, tens of thousands of PV water submersible pumps were deployed globally<sup>13</sup>. In 1998, this installation had grown to about 60,000 installations<sup>14</sup>. Pumping water requires the development of a unique machine valve. Since 1968, solar photovoltaic generators have been used in several regions of the world, including SWP<sup>15</sup>. The massive solar water pump was constructed in 1901 in Pasadena, California, USA<sup>16</sup>. Next, Harrington of New Mexico was the first to employ CSP to divert water up to 6 m high in 1920. Finally, the literature research demonstrated that SWP utilised PV and CSP to complete its tasks. Parabolic trough solar collection (PTSC) is another form of CSP in which heat transfer fluid (HTF) transports warmth from the hoarder to the heat exchanger to create power<sup>17</sup>. HTF in PTSC can reach 390 °C in temperature, and it also has these characteristics: low viscosity, pressure, cooling, and storage cost; non-corrosive; and proven to be safe<sup>18</sup>. Nanofluids have recently been revealed to be particular HTFs with great insulation characteristics. The supreme common nano-materials in nano-fluid are metal and non-metal. Carbon nanotubes (CNT), mono carbon nanotubes (SWCNT), and multi-walled carbon nanotubes (MWCNT) are among the nano-fluid particles included in the computational model and experimental studies in PTSC<sup>19</sup>.

The Oldroyd-B model is a fundamental ideal cast-off to describe the flow of viscoelastic fluid, named after its creator Oldroyd<sup>20</sup>. The Oldroyd-B model was developed by Irfan et al.<sup>21</sup> to analyse the blood flow, and they recommended that the viscoelastic property in blood should be considered, especially when the shear values are low. Subsequently, the analytical and numerical models of Oldroyd-B viscoelastic fluid have been reported<sup>22–24</sup>. According to Sajid et al.<sup>22</sup>, using a method of regional variance, the computational complexity for the circulation of the Oldroyd-B aqueous flow separation in a stance phase goes beyond a stretch sheet. The effect of thermal radiation, Joule heating, magnetic field, and thermophoresis has been described by Hayat and Alsaedi<sup>23</sup>. The analytical model in the capillary under the Debye-Hückel approximation, with the effect of electro-osmotic flow, was solved by Zhao et al.<sup>24</sup>.

Mixed nano-fluids are novel nano-fluids prepared by forming different nanoparticles in combination or composite form. The impetus for the preparation of composite nano-fluids is the continuous upgrading of warmth transmission with the improved thermal conductivity of these nano-fluids. Among all the hybrid nano-fluids tested, CNT/Fe<sub>3</sub>O<sub>4</sub> nano-fluid are widely analysed. Baby and Sundara<sup>25</sup> reported improvements in thermal performance of 3–5% and 6.5–10% at 0.005% and concentration of 0.03% CNT/Fe<sub>3</sub>O<sub>4</sub> hybrid nano-fluid with a thermal reading of 30–50 °C. This nano-fluid reveals a non-Newtonian demeanour in more than 6% voltages, and its viscosity decreases as temperatures rise. At a temperature of 30–60 °C and the nanoparticles volume ratios of 0–1%, the ethylene glycol/MgO-MWCNT mixture nano-fluid density was reported by Soltani and Akbari<sup>23</sup>. A non-Newtonian composite nanofluid comprising CNT/Fe<sub>3</sub>O<sub>4</sub> coated nanoparticles is used as a cooler in a short channel temperature changer, and the viscosity and thermal conductivity were measured<sup>26</sup>. In that process, to synthesize nano-fluid mixtures, pure ferrofluid was first produced in the manner presented by Berger et al.<sup>27</sup>. Then, CNT nano-fluid was prepared using the method suggested by Garg et al. It is noteworthy that TMAH and GA were used respectively to coagulate Fe<sub>3</sub>O<sub>4</sub> nanoparticles and CNTs to prevent particle coagulation. In the next step, the hybrid nano-fluid was produced by adding the required amount of CNT nano-fluid to the ferrofluid produced, followed by the sonication of the mixture. Recent works can be found in<sup>27–31</sup>.

Buongiorno proposed a non-homogeneous nano-fluid model, where the random movement of nanoparticles and thermo-diffusion effect was found to be the most contributing factors<sup>32</sup>. The modified Buongiorno model for partial volume analysis is used to study the bioconvective flow of gyrotactic microorganisms<sup>33</sup>. Rawat et al.<sup>34</sup> applied the improved Buongiorno's Ideal to consider the consequence of chemical and radiation reactions on the magnetic nano-fluid flow bounded in a cone. Rana et al.<sup>35</sup> chose alumina and titania particles in their Buongiorno's model, whereas the volatile transport of hybrid nano-fluid over long distances was examined by Ali et al.<sup>36</sup>. As a result, the random movement of the nanoparticles in<sup>32–36</sup> is known as the Brownian movement<sup>37</sup>. The pioneer experimental study of Brownian motion observed the coal dust particles in the alcohol<sup>38</sup> and pollen grains in the water<sup>39</sup>. Besides, Albert Einstein formed the mathematical model of the Brownian movement. Garg and Jayaraj<sup>40</sup> recently pronounced the vaporizer atom movement and the thermophoresis effect in cylindrical geometry.

Thermal radiation is one type of heat transmission in the form of electromagnetic waves when the bodies in the same system are not in direct physical contact with each other<sup>41</sup>. The bodies with higher absolute zero temperatures will be able to emit thermal radiation<sup>42</sup>. The applications of thermal radiation were observed in ultrasound-assisted and microwave-assisted heating methods<sup>43</sup>. The presence of nanoparticles in the nanofluid, on the other hand, boosts the thermal conductance of the nano-fluid itself, with a minimum percentage of 12%. As a result, measuring variation in the fluidity of nanofluid in conceptual or observational correlations was discovered to be particularly essential<sup>44</sup>. The thermophysical properties of hybrid nano-fluid (more than one nanoparticle in the base fluid) were reported<sup>45,46</sup>, where Adriana<sup>45</sup> solved the fluid model numerically and Afrand et al.<sup>46</sup> worked on their model by experimenting.

A chemical reaction is a chemical transformation process from one chemical substance to another. The positions of the electrons are changed, and chemical bonds between atoms will be broken in this reaction<sup>47</sup>, and it can be represented by a chemical equation<sup>48</sup>. The first-order substance response in the fluid flow model was studied by Chambre and Young<sup>49</sup> and Ramanamurthy and Rao<sup>50</sup> for the case of static horizontal plates<sup>49</sup> and cylindrical catalyst pellets<sup>50</sup>. The thermal properties of hybrid nano-fluid beyond a tempestuous exterior

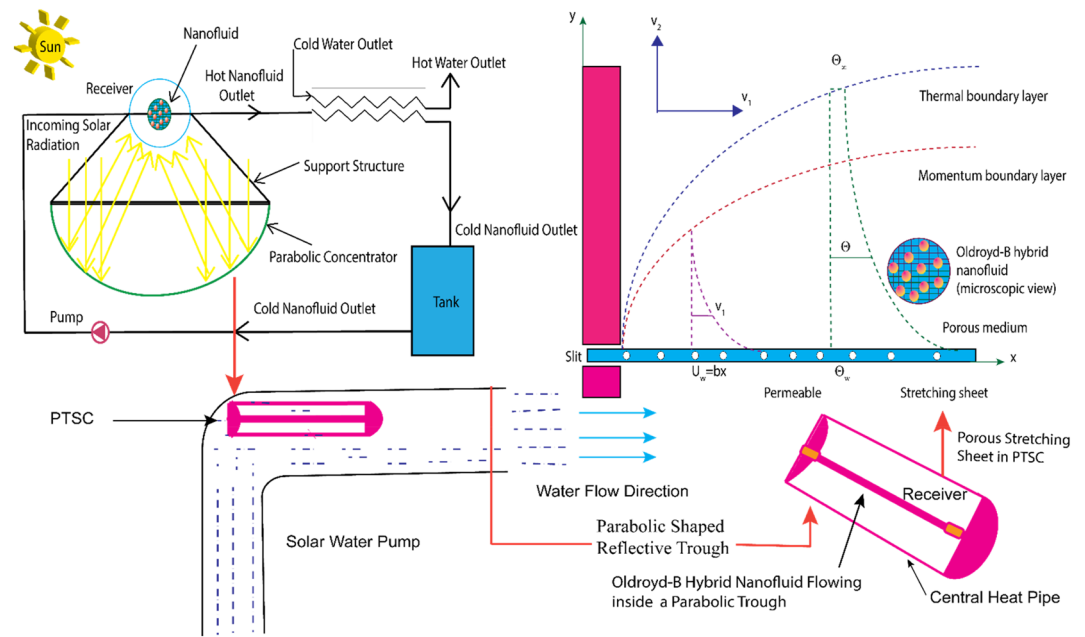


**Figure 1.** Schematic display of SWP.

were described by Nadeem et al.<sup>51</sup> and Yusuf et al.<sup>52</sup>. Nadeem et al.<sup>51</sup> deliberate the movement of the nano-fluid mixture. In contrast, the radiating nano-fluid and hybrid nano-fluid by the presence of Darcy–Forchheimer absorbent media is studied by Yusuf et al.<sup>52</sup>. Mabood et al.<sup>53</sup> describe the transmission of temperature and mass in nanofluid beyond a spinning frame. Subsequently, articles regarding the warmth transmission and the movement of nano-fluid and hybrid nano-fluid have been published under the effect of velocity slip<sup>54</sup>, entropy<sup>54</sup>, radiation<sup>55,56</sup>, and melting process<sup>55,56</sup>. Furthermore, heat transmission in a liquid nanopore confined by a lateral molten surface is observed<sup>57,58</sup>.

Entropy is a measured quantity related to a state of distraction, disorder, or uncertainty. Ludwig Boltzmann, a well-known Austrian physicist, defined enthalpy as the evaluation of conformance amongst tiny processes (including individual atoms and molecules) and macroscopic systems<sup>59</sup>. The addition of nanoparticles to essential fluids can contribute to the entire generation of entropy<sup>60</sup>. As a result, the incorporation of nanoparticles in the base fluid improves the nano-fluid viscosity and reduces the pressure in the thermal system. Furthermore, the job of nano-fluids is to lower the temperature of the heat pipe, which minimises the amount of heat transmitted to the overall amount of entropy creation. Sciacovelli et al.<sup>61</sup> studied the applicability of entropy production to numerous engineering domains. At the same time, Manjunath and Kaushik<sup>62</sup> reported second-law entropy generation in the operation of the heater. The model of entropy generation in pore systems is developed by Torabi et al.<sup>63</sup>. Subsequently, Mahian et al.<sup>64</sup> deal with entropy generation in nano-fluid/hybrid nano-fluid flow. The entropy production rate has been found to upsurge in a high concentration of nanoparticles due to the presence of contrasting forces<sup>65</sup>.

Heat transfer analysis researchers are concentrating their efforts on coming up with a timely solution to this problem due to the increasing need for heat management caused by overheating heating systems for various technological and industrial operations. By taking this into account, this study investigates the thermal performance of a solar water pump (SWP) employing mono/hybrid nano-fluids (AA7075–EO and AA7075–Ti–6Al–4 V/EO), as well as a parabolic trough solar collector (PTSC) situated within an SWP. Solar radiation is considered a heat source. The schematic diagram is depicted in Fig. 1. Demonstrates sun-based radiation and the existence of a heat source in a technique to improve the efficacy of a solar water pump (SWP) using sunlight-based radiation and nanotechnology. The study is organized to examine the heat kinetics of the SWP using mono- and hybrid nanofluidic (PTSC) nanofluids located in the SWP as coolant liquid. The radiation directed at the sun is a source of heat. The implementation of heat exchange is examined for the effects of various parameters such as radiation, chemical reaction, porousness material, as well as thermal dissipation. The pump's thermal transfer performance is described for various features, for example, warmth cause, thermal radiation, and viscid dissipation. Entropy propagation examination has been analysed for the movement of Oldroyd-B hybrid nanofluid. To handle the formulation, we've chosen the Keller box method (KBM) as our primary solution strategy. Figures and tables show the effects of various factors such as fluid velocity, fluid temperature, measurement of exterior drag, and Nusselt number.

The introduction and the mathematical formulation are positioned in Sect. “Introduction” and Sect. “Mathematical Formulation”, respectively. Section “Problem Solution” discussed the subsequent model equations. Sequentially, the solution and employment of numerical methodology are included in Sects. “Entropy Generation Analysis” and “Employment of Numerical Methodology: KBM”. The code validation, results, and discussion are

Aspects	Nano-fluid	Hybrid nanofluid
Viscosity ( $\mu$ )	$\mu_{nf} = \mu_f(1 - \phi)^{-2.5}$	$\mu_{hnf} = \mu_f(1 - \phi_{p1})^{-2.5}(1 - \phi_{p2})^{-2.5}$
Density ( $\rho$ )	$\rho_{nf} = (1 - \phi)\rho_f - \phi\rho_s$	$\rho_{hnf} = [(1 - \phi_{p2})\{(1 - \phi_{p1})\rho_f + \phi_{p1}\rho_{p1}\}] + \phi_{p2}\rho_{p2}$
Heat capacity ( $\rho C_p$ )	$(\rho C_p)_{nf} = (1 - \phi)(\rho C_p)_f - \phi(\rho C_p)_s$	$(\rho C_p)_{hnf} = [(1 - \phi_{p2})\{(1 - \phi_{p1})(\rho C_p)_f + \phi_{p1}(\rho C_p)_{p1}\}] + \phi_{p2}(\rho C_p)_{p2}$
Thermal conductivity ( $\kappa$ )	$\frac{\kappa_{nf}}{\kappa_f} = \left[ \frac{(\kappa_s + 2\kappa_f) - 2\phi(\kappa_f - \kappa_s)}{(\kappa_s + 2\kappa_f) + \phi(\kappa_f - \kappa_s)} \right]$	$\frac{\kappa_{hnf}}{\kappa_f} = \left[ \frac{(\kappa_{p2} + 2\kappa_{nf}) - 2\phi_{p2}(\kappa_{nf} - \kappa_{p2})}{(\kappa_{p2} + 2\kappa_{nf}) + \phi_{p2}(\kappa_{nf} - \kappa_{p2})} \right], \frac{\kappa_{nf}}{\kappa_f} = \left[ \frac{(\kappa_{p1} + 2\kappa_f) - 2\phi_{p1}(\kappa_f - \kappa_{p1})}{(\kappa_{p1} + 2\kappa_f) + \phi_{p1}(\kappa_f - \kappa_{p1})} \right]$

**Table 1.** Thermophysical aspects of the Oldroyd-B fluid.

consecutively in Sects. “Code Validity” and “Results and Discussion”. Finally, Sect. “Final Outcomes” summarises the outcomes.

It is presented a theoretical investigation to improve the efficiency of SWP by utilising the benefits of a hybrid nanofluid’s thermal characteristics over a PTSC. The PTSC was determined to be installed in many positions in SWP. The following are the current research’s objectives:

- In this model, PVC cell sheets (as reported from the previous model of SWP) have been replaced with PTSC.
- The PTSC cylinder-shaped system has a broader exterior area than PVC sheets, allowing it to capture more solar energy.
- SWP has a low production and maintenance cost due to solar energy usage.
- According to the interpretation, the accumulation of nano-materials into the base fluid intensifies the thermal transmission through PTSC by generating additional energy.
- SWP does not contaminate the air, and it is also environmentally friendly.
- SWP is useful in third-world or developing nations where alternative sources of energy or water are unavailable.

### Mathematical formulation

Equation 1 denotes the extended straight flat exterior with the speed  $U_w$ , where  $b$  is a positive constant<sup>17</sup>.

$$U_w(x, 0) = bx. \tag{1}$$

The governing equations below (Eqs. 2–5) represent the viscous hybrid nano-fluid Oldroyd-B flow near the penetrable surface. This model also being affected by viscous dissipation and heat sources<sup>66</sup>.

$$\frac{\partial v_1}{\partial x} + \frac{\partial v_2}{\partial y} = 0, \tag{2}$$

$$v_1 \frac{\partial v_1}{\partial x} + v_2 \frac{\partial v_1}{\partial y} + \lambda_1 \left[ v_1^2 \frac{\partial^2 v_1}{\partial x^2} + v_2^2 \frac{\partial^2 v_1}{\partial y^2} + 2v_1 v_2 s \frac{\partial^2 v_1}{\partial x \partial y} \right] = \frac{\mu_{hnf}}{\rho_{hnf}} \left[ \left( \frac{\partial^2 v_1}{\partial y^2} \right) - \frac{v_1}{k} \right] + \frac{\mu_{hnf}}{\rho_{hnf}} \left[ \lambda_2 \left( v_1 \left( \frac{\partial^3 v_1}{\partial x \partial y^2} \right) - \frac{\partial v_1}{\partial x} \left( \frac{\partial^2 v_1}{\partial y^2} \right) + \frac{\partial v_1}{\partial y} \left( \frac{\partial^2 v_2}{\partial y^2} \right) + v_2 \left( \frac{\partial^3 v_1}{\partial y^3} \right) \right) \right], \tag{3}$$

$$v_1 \frac{\partial \Theta}{\partial x} + v_2 \frac{\partial \Theta}{\partial y} = \frac{k_{hnf}}{(\rho C_p)_{hnf}} \left( \frac{\partial^2 \Theta}{\partial y^2} \right) - \frac{1}{(\rho C_p)_{hnf}} \left( \frac{\partial q_r}{\partial y} \right) + \frac{1}{(\rho C_p)_{hnf}} Q(\Theta - \Theta_\infty) + \frac{\mu_{hnf}}{(\rho C_p)_{hnf}} \left( \frac{\partial v_1}{\partial y} \right)^2, \tag{4}$$

$$v_1 \frac{\partial C^*}{\partial x} + v_2 \frac{\partial C^*}{\partial y} = D_B \frac{\partial^2 C^*}{\partial y^2} + \frac{D_T}{T_\infty} \left( \frac{\partial^2 \Theta}{\partial y^2} \right) - k_1(C^* - C_\infty^*). \tag{5}$$

The respective boundary conditions shall be<sup>67</sup>:

$$\left. \begin{aligned} v_1(x, 0) = U_w + N_w \left( \frac{\partial v_1}{\partial y} \right), v_2(x, 0) = V_w, -k_0 \left( \frac{\partial \Theta}{\partial y} \right) = h_f(\Theta_w - \Theta), C^*(x, 0) = C_w^*, \\ v_1 \rightarrow 0, \frac{\partial v_1}{\partial y} \rightarrow 0, \Theta \rightarrow \Theta_\infty, C^* \rightarrow C_\infty^* \text{ as } y \rightarrow \infty. \end{aligned} \right\} \tag{6}$$

The vector of fluid velocity is expressed as  $\vec{v} = [v_1(x, y, 0), v_2(x, y, 0), 0]$ . Meanwhile, these symbols:  $\Theta$ ,  $N_w$ ,  $V_w$ , and  $k$  were consistently noted as fluid temperature, slip length, stretching porousness surface, and material porousness. The characteristics of thermo-physical are intensified when the nano-sized particles are diffused in the base fluid.

The thermophysical formulation of Oldroyd-B nano-fluid, such as viscosity, density, heat capacity, and thermal conductivity, is shown in the second column of Table 1<sup>68</sup>. Besides, Oldroyd-B hybrid nano-fluid is displayed in the third column of Table 1<sup>69</sup>. The combination of dual diverse nanoparticles in a standard fluid causes an augmentation of heat transmission for the whole fluid.

The symbols as displayed in Table 1 ( $\rho$ ,  $\mu$ ,  $\kappa$ , and  $C_p$ ) are denoted sequentially as density, hybrid nano-fluid dynamical viscidness, thermal conductance, and specific heat capacitance. All of these symbols have subscripts  $f$ ,  $s$ ,  $nf$ ,  $hnf$ ,  $p_1$  and  $p_2$ . They are declared as the base fluid, solid nanoparticle, nano-fluid, hybrid nano-fluid,

Thermophysical	$\rho$ (kg/m <sup>3</sup> )	$c_p$ (J/kgK)	$k$ (W/mK)
Ti-6Al-4V (titanium alloy)	4420	0.56	7.2
Engine Oil (EO)	884	1910	0.144
AA7075 (aluminum alloy)	2810	960	173

**Table 2.** Base fluid and nano-sized particles with 293 K significant properties.

first solid nanoparticle, and second solid nanoparticle, respectively. Moreover,  $\phi$  defines as the concentration factor of nano-fluid and  $\phi_h = \phi_{p_1} + \phi_{p_2}$  is expressed as the total concentration factor of hybrid nano-fluid due to the mixture of dual nanoparticles. The thermophysical values of the base fluid, together with their nano-sized particles, are presented in Table 2<sup>70,71</sup>.

The Rosseland approximation<sup>72</sup> can be written as

$$q_r = -\frac{4\sigma^*}{3k^*} \frac{\partial \Theta^4}{\partial y}, \tag{7}$$

where  $q_r$ ,  $\sigma^*$ , and  $k^*$  signifies the thermal radiative parameter, Stefan Boltzmann constant, and absorption coefficient.

**Problem solution**

The boundary values problem contains Eqs. (2–6) have been converted to ODEs (Eqs. 10–13) after implementing the similarity approach (Eq. 9). The first step is to produce the velocity in the  $x$ - and  $y$ - components from stream function  $\psi$ , as shown in Eq. 8 (See, Ref<sup>17</sup>).

$$v_1 = \frac{\partial \psi}{\partial y}, v_2 = -\frac{\partial \psi}{\partial x}. \tag{8}$$

$$\omega(x, y) = \sqrt{\frac{b}{v_f}} y, \psi(x, y) = \sqrt{v_f b x} F(\omega), \theta(\omega) = \frac{\Theta - \Theta_\infty}{\Theta_w - \Theta_\infty}, h = \frac{C^* - C_\infty^*}{C_w^* - C_\infty^*}. \tag{9}$$

$$F''' + \Psi_a \Psi_b [FF'' - F'^2 + \alpha_1 (2FF' - F^2 F''')] + \alpha_2 (F''^2 - FF^{iv}) - \frac{1}{\phi a} KF' = 0, \tag{10}$$

$$\theta'' \left( 1 + \frac{1}{\Psi_d} Pr N_r \right) + Pr \frac{\Psi_c}{\Psi_d} \left[ F\theta' - F'\theta + \theta \frac{Q}{\Psi_c} + \frac{E_c}{\Psi_a \Psi_c} F'^2 \right] = 0, \tag{11}$$

$$h'' + Pr Sc F h' + \frac{Nt}{Nb} \theta'' - Sc \varkappa h = 0. \tag{12}$$

with

$$\left. \begin{aligned} f(0) = S, f'(0) = 1 + \gamma^* f''(0), \theta'(0) = -Bi(1 - \theta(0)), h(0) = 1 \\ f'(\infty) \rightarrow 0, f''(\infty) \rightarrow 0, \theta(\infty) \rightarrow 0, h(\infty) \rightarrow 0. \end{aligned} \right\} \tag{13}$$

Here  $\Psi_i$ 's with  $1 \leq i \leq 4$  in Eqs. (10) and (11) indicate thermophysical properties for Oldroyd-B hybrid nano-fluid as Eqs. (14–16):

$$\Psi_a = (1 - \phi_R)^{2.5} (1 - \phi_H)^{2.5}, \Psi_b = (1 - \phi_H) \left\{ (1 - \phi_R) + \phi_R \frac{\rho_{p1}}{\rho_f} \right\} + \phi_H \frac{\rho_{p2}}{\rho_f}, \tag{14}$$

$$\Psi_c = (1 - \phi_H) \left\{ (1 - \phi_R) + \phi_R \frac{(\rho C_p)_{p1}}{(\rho C_p)_f} \right\} + \phi_H \frac{(\rho C_p)_{p2}}{(\rho C_p)_f}, \tag{15}$$

$$\Psi_d = \left[ \frac{(\kappa_{p2} + (m - 1)\kappa_{gf}) - (m - 1)\phi_H(\kappa_{gf} - \kappa_{p2})}{(\kappa_{p2} + (m - 1)\kappa_{gf}) + \phi_H(\kappa_{gf} - \kappa_{p2})} \right] \left[ \frac{(\kappa_{p1} + (m - 1)\kappa_f) + \phi_R(\kappa_f - \kappa_{p1})}{(\kappa_{p1} + (m - 1)\kappa_f) - (m - 1)\phi_R(\kappa_f - \kappa_{p1})} \right]. \tag{16}$$

The notation (') in Eqs. (10–13) indicates the derivatives concerning  $\xi$ . The parameters involved are listed as follows:  $\alpha_1 = bQ_1$  (Deborah number-I),  $\alpha_2 = bQ_2$  (Deborah number-II),  $K = \frac{\nu_f}{bk}$  (porous medium parameter),  $Pr = \frac{\nu_f}{\alpha_f}$  (Prandtl number),  $\alpha_f = \frac{\kappa_f}{(\rho C_p)_f}$  (thermal diffusivity),  $S = -V_w \sqrt{\frac{1}{v_f b}}$  (mass transfer),  $N_r = \frac{16}{3} \frac{\sigma^* \Theta_\infty^3}{\kappa^* \nu_f (\rho C_p)_f}$  (thermal radiation),  $E_c = \frac{U_w^2}{(C_p)_f (\Theta_w - \Theta_\infty)}$  (Eckert number),  $\gamma^* = \sqrt{\frac{b}{v_f}} N_w$  (velocity slip),  $\varkappa = \frac{k_1}{b}$  (chemical reaction

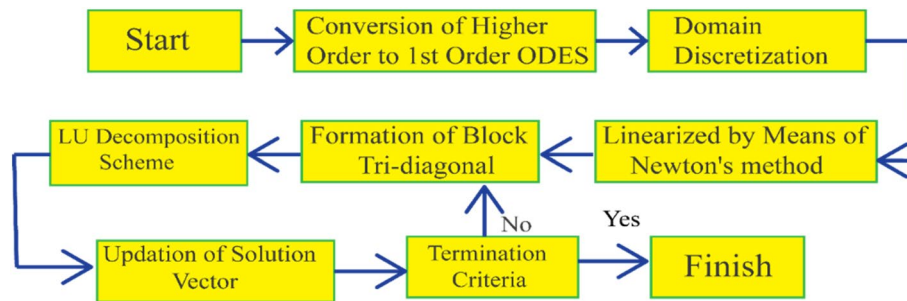


**Figure 2.** Diagram of clarifying Keller box scheme.

parameter), and  $Bi = \frac{h_f}{k_0} \sqrt{\frac{v_f}{b}}$  (Biot number). The physical interest quantities in this model are the local Nusselt number  $Nu_x$  and the mass transport rate  $Sh_x$ :

$$Nu_x = \frac{xq_w}{k_f(w - \infty)}, Sh_x = \frac{xq_m}{D_B(h_w - h_\infty)} \tag{17}$$

wherein the flux with the components of heat  $q_w$  and the mass  $q_m$  are expressed as

$$q_w = -k_{hmf} \left( 1 + \frac{16}{3} \frac{\sigma_\infty^3}{\kappa * v_f (\rho C_p)_f} \right) \left( \frac{\partial}{\partial y} \right)_{y=0}, q_m = -D_B \left( \frac{\partial C^*}{\partial y} \right) \tag{18}$$

The above equations (Eqs. 17–18) will be transformed as below, with the involvement of the similarity approach (Eq. 9):

$$Nu_x Re_x^{-\frac{1}{2}} = -\frac{k_{hmf}}{k_f} (1 + Nr) \theta'(0), Sh_x Re_x^{-1/2} = -h'(0) \tag{19}$$

where local Reynolds number  $Re_x$  is expressed as  $Re_x = \frac{U_w x}{v_f}$ .

### Entropy generation analysis

The entropy generation can be shown in Eq. (20)<sup>73</sup>:

$$E_G = \frac{k_{hmf}}{2_\infty} \left\{ \left( \frac{\partial}{\partial y} \right)^2 + \frac{16}{3} \frac{\sigma_\infty^3}{\kappa * v_f (\rho C_p)_f} \left( \frac{\partial}{\partial y} \right)^2 \right\} + \frac{\mu_{hmf}}{\infty} \left( \frac{\partial v_1}{\partial y} \right)^2 + \frac{\mu_{hmf} v_1^2}{k_\infty} \tag{20}$$

The dimensionless entropy equation is formulated as<sup>74</sup>,

$$N_G = \frac{2_\infty b^2 E_G}{k_f (w - T_\infty)^2} \tag{21}$$

However, Eq. (20) is transformed as below due to the usage of Eq. (11):

$$N_G = Re \left[ \Psi_d (1 + Nr) \theta'^2 + \frac{1}{\Psi_a} \frac{Br}{\Omega} (f'^2 + Kf'^2) \right] \tag{22}$$

### Employment of numerical methodology: KBM

The numerical solutions of Eqs. (10–12), together with the endpoint condition (13), can be recorded by utilising the Keller box method (KBM)<sup>75</sup> developed in MATLAB software. The flow chart of KBM is displayed in Fig. 2.

The higher-order ODEs must be converted to the first-order ODEs, which will produce the new substitutions implemented in the KBM. Dependent variables  $e_i$ , with  $1 \leq i \leq 8$  are introduced as below:

$$e_1 = F, e_2 = F', e_3 = F'', e_4 = F''', e_5 = \theta, e_6 = \theta', e_7 = h, e_8 = h'. \tag{23}$$

$$\frac{de_1}{d\omega} = e_2, \tag{24}$$

$$\frac{de_2}{d\omega} = e_3, \tag{25}$$

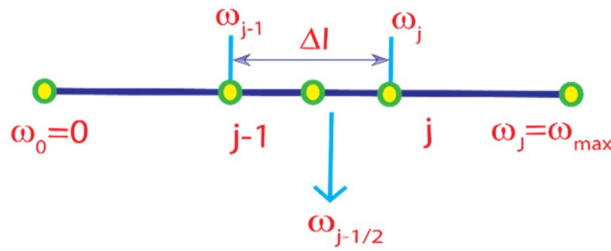


**Figure 3.** Standard grid structure for the difference approximations method.

Pr	Ref. <sup>17</sup>	Ref. <sup>76</sup>	Ref. <sup>77</sup>	Ref. <sup>78</sup>	Ref. <sup>79</sup>	Ref. <sup>80</sup>	Present
0.72	0.80876181	0.8086	0.8086	0.80863135	0.80876122	0.80876181	0.80876181
1.0	1.0	1.0	1.0	1.0	1.0	1.0	1.0
3.0	1.92357420	1.9237	1.9236	1.92368259	1.92357431	1.92357420	1.92357420
7.0	3.07314651	3.0723	3.0722	3.07225021	3.07314679	3.07314651	3.07314651
10	3.72055429	3.7207	3.7006	3.72067390	3.72055436	3.72055429	3.72055429

**Table 3.** The comparison of  $-\theta'(0)$  values with the increasing Prandtl Number,  $\phi = 0, \phi_h = 0, Q = 0, \gamma^* = 0, E_c = 0, N_r = 0, Q = 0, E_c = 0, S = 0,$  and  $Bi = 0.$

$$\frac{de_3}{d\omega} = e_4, \tag{26}$$

$$\frac{de_5}{d\omega} = e_6, \tag{27}$$

$$\frac{de_7}{d\omega} = e_8, \tag{28}$$

$$-\alpha_2 e_1 \frac{de_4}{d\omega} + \alpha_2 e_3^2 + \Psi_a \Psi_b e_1 e_3 - \Psi_a \Psi_b e_2^2 + 2\Psi_a \Psi_b \alpha_1 e_1 e_2 - \Psi_a \Psi_b \alpha_1 e_1^2 e_4 - \frac{1}{\Psi_a} K e_2 + e_4 = 0, \tag{29}$$

$$\frac{de_6}{d\omega} + \frac{1}{\Psi_d} PrNr \frac{de_6}{d\omega} + Pr \frac{\Psi_c}{\Psi_d} e_1 e_6 - Pr \frac{\Psi_c}{\Psi_d} e_2 e_5 + \frac{PrQ}{\Psi_d} e_5 + \frac{PrEc}{\Psi_a \Psi_d} e_3^2 = 0, \tag{30}$$

$$\frac{de_8}{d\omega} + PrSce_1 e_8 + \frac{Nt}{Nb} \frac{de_6}{d\omega} - Sc\chi e_7 = 0, \tag{31}$$

$$\left. \begin{aligned} e_1(0) = S, e_2(0) = 1 + \gamma^* e_3(0), e_6(0) = -Bi(1 - e_5(0)), e_7(0) = 1, \\ e_2(\infty) \rightarrow 0, e_3(\infty) \rightarrow 0, e_5(\infty) \rightarrow 0, e_7(\infty) \rightarrow 0. \end{aligned} \right\} \tag{32}$$

The domain  $[0, 1]$  has been transformed into sub-domains, with a regular mesh, together with the subsequent grid points (Fig. 3):

$\omega_0 = 0, \omega_j = \omega_{j-1} + \Delta I, j = 0, 1, 2, 3, \dots, J, \omega_J = 1$  where  $\Delta I$  is the step size (as attached in Appendix A). For the above calculation, a mesh size of  $\Delta I = 0.01$  is chosen, and the results are recognized to have an error tolerance by  $10^{-6}$ .

**Code validity**

The results validation has been done by making a comparison with the previously published reports <sup>17,76–80</sup>, as shown in Table 3. The consistent values until six decimal places have been presented for all results proved that the current technique KBM is accepted, and the investigation can go further. Furthermore, the results produced by the recently founded Keller-Box approach correspond well with those obtained by MATLAB’s built-in solver `bvp4c`.

**Results and discussion**

This section includes graphical interpretations of velocity  $F'(\omega)$  (as shown in Figs. 6, 9, 12, 15, 18, 26, 29), temperature  $\theta(\omega)$  (as depicted in Figs. 7, 10, 13, 16, 21, 23, 24, 25, 27, 30) concentration  $h(\omega)$  and entropy  $\frac{N_G}{N_G}$  (Figs. 4, 5, 8, 11, 14, 17, 19, 20, 22, 27, 31, 32, 33). In addition to the plots, the rate of Nusselt number ( $N_u Re_x^{-2}$ )



$\alpha_1$	$\alpha_2$	$\phi/\phi_h$	$S$	$Q$	$N_r$	$Bi$	$Ec$	$\gamma^*$	$K$	$N_u Re_x^{-1}$ mono	$N_u Re_x^{-1}$ hybrid	Relative $\frac{Nu_{hybrid} - Nu_{nano}}{Nu_{hybrid}} \times 100$
0.1	0.1	0.02	0.1	0.1	0.1	0.1	1.0	0.1	0.1	0.08041	0.10582	24.21%
0.2										0.08078	0.11885	32.12%
0.3										0.08139	0.12706	35.21%
	0.1									0.08041	0.10582	24.21%
	0.2									0.08095	0.11632	30.31%
	0.3									0.08106	0.12372	34.37%
		0.02								0.08041	0.10582	24.21%
		0.06								0.08048	0.10799	25.48%
		0.1								0.08084	0.10994	26.37%
			0.1							0.08041	0.10582	24.21%
			0.3							0.08060	0.10699	24.66%
			0.5							0.08080	0.10809	25.14%
				0.1						0.08041	0.10582	24.21%
				0.3						0.08080	0.10699	24.47%
				0.5						0.08139	0.10978	25.75%
					0.1					0.08041	0.10582	24.21%
					0.2					0.08133	0.10796	24.48%
					0.3					0.08244	0.10999	25.15%
						0.1				0.08041	0.10582	24.21%
						0.2				0.08080	0.10799	25.17%
						0.3				0.08085	0.10891	25.76%
							1			0.08041	0.10582	24.21%
							3			0.08050	0.10691	24.70%
							5			0.08066	0.10777	25.15%
								0.1		0.08041	0.10582	24.21%
								0.3		0.08040	0.10482	23.29%
								0.5		0.08039	0.10382	22.56%
									0.1	0.08041	0.10582	24.21%
									0.2	0.08047	0.10784	25.28%
									0.3	0.08052	0.10892	26.25%

**Table 4.** Calculation of Nusselt Number =  $N_u Re_x^{-1}$  for  $Pr = 6450$ .

are depicted in Fig. 32 as well as Table 4. Numerical computations are done for controlling factors, which include both components of Deborah's number  $\alpha_1$  and  $\alpha_2$ , slip velocity  $\gamma^*$ , a factor of porous media  $K$ , volume friction of nanoparticles  $\phi$ , viscous dissipation  $Ec$ , Biot number  $Bi$ , radiation factor  $N_r$ , heat source  $Q$ , suction ( $S > 0$ ), Reynolds number  $Re$ , injection ( $S < 0$ ), chemical reaction  $\chi$  as well as Brinkman number  $B_r$ . Comparison between mono nano-fluid (AA7075/EO) with hybrid nano-fluid (AA7075–Ti–6Al–4 V/EO) has been shown with numerical outcomes about temperature, velocity, entropy as well as Nusselt number. A solid line represents mono nano-fluid and hybrid nano-fluid by dashed lines.

As shown in Fig. 4, increasing the value of the chemical reaction parameter causes a rapid suppression in  $h(\omega)$ . When a chemical reaction is improved, many molecules are used, and a low chance of involvement in the mass transfer is provided. Mass dispersion is decreased as a result of this restriction.

As shown in Fig. 5, a sudden increase in Schmidt number caused a decrement in nano-fluid concentration. As a result, the rate of molecular diffusion is reduced. Furthermore, a decrease in nano-fluid concentration reduced mass transfer in the system. Physically, the mass transference boundary layer and the hydrodynamic layer's relative thickening are connected to a decrease in concentration.

Deborah number  $\beta$  is a dimensionless number that is used to measure the physical property of the fluid. Influence of  $\beta_1$  regarding changes in  $F'(\omega)$ ,  $\theta(\omega)$ , and  $N_G$  are represented in Figs. 6, 7, 8, respectively. Effects concerning  $\beta_2$  regarding changes in  $F'(\omega)$ ,  $\theta(\omega)$ , and  $N_G$  are depicted in Figs. 9, 10, 11. A deceleration in velocity is observed regarding  $\beta_1$  while the increment is a result of  $\beta_2$ . But the opposite reaction to velocity is obtained when it comes to temperature, regarding the same Deborah parameters  $\beta_1$  and  $\beta_2$ . However, entropy is decreased components of Deborah's number are increased, as shown in Figs. 8 and 11. The model of non-linear Oldroyd-B fluid is appropriately depicted as simple "Boger" fluid. This fluid contains a mixture of a dilute suspended of high molecular weight polymers and a high viscosity solvent. While it captures elastic responses, it does not capture the shear-thinning effect of the polymer.

When the increment is done in values of  $K$ , the fields of  $F'(\omega)$ ,  $\theta(\omega)$ , and  $N_G$  are depicted in Figs. 12, 13, 14. When the porosity parameter enhances, the thermal boundary layer is enlarged. Consequently,  $\theta(\omega)$  and  $N_G$  become risen. However, the fluid velocity declined due to the same parameter. A consequence of  $\phi$  on these

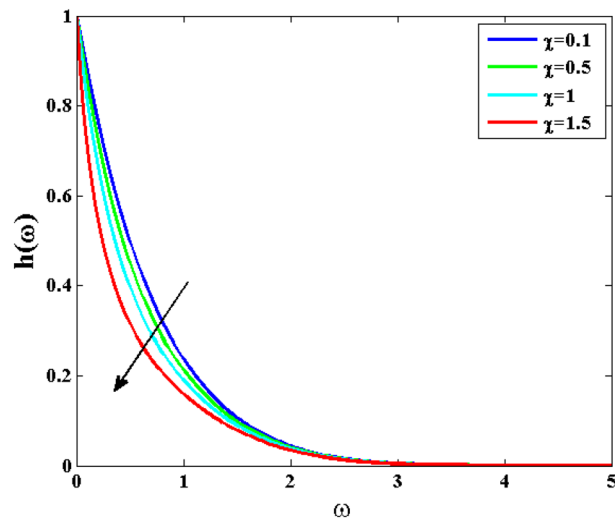


**Figure 4.** Graph of concentration with increasing  $\chi$ .

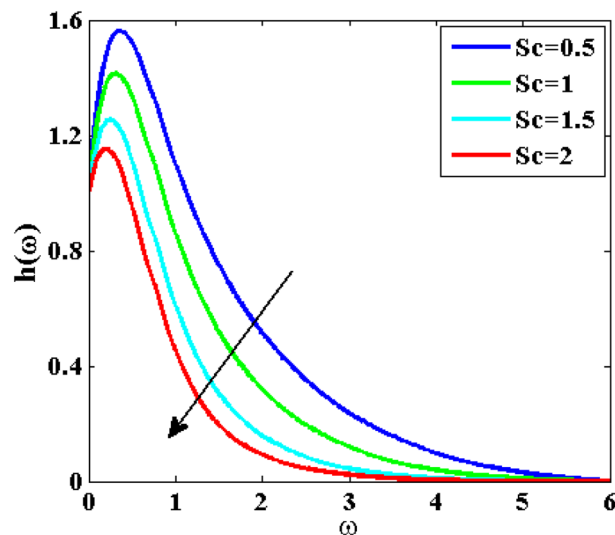


**Figure 5.** Graph of concentration with increasing  $Sc$ .

profiles can also be observed in Figs. 15, 16, 17. Parameters  $K$  and  $\phi$  resulted in the increment of temperature and entropy profiles. Simultaneously, parameters  $K$  and  $\phi$  cause the velocity to reduce. The presence of porous media  $K$  is to restrict the fluid motion. Hence the speed will be diminished. In addition, the increase of nanoparticles volume  $\phi$  produces frictional force in fluid, which resists fluid movement. Due to the growth in thermal conducting, the width of the temperature boundary layer increased as a result of the increasing volume of nanomolecules. This is justified by the fact that the fluids' thermal characteristics are enhanced by the rise in nanomolecules concentration. Additionally, the conventional fluid and nanomolecule combination enhances heat conduction across the entire liquid, raising the temperature outline.

The slip effect  $\gamma^*$  on the plate decelerates the velocity of the fluid, causing the speed to become diminished. At the same time, the thickness of the entropy component for the boundary layer becomes thinner by increasing  $\gamma^*$ . The diminution of the velocity and entropy profiles are subjected to the increment of  $\gamma^*$ , as shown consecutively in Figs. 18 and 19. The thermal boundary layer becomes broad with the effect of  $\gamma^*$  (Fig. 20).

Variations in  $\theta(\omega)$  and  $N_G$  for various values of  $Bi$ ,  $Q$ ,  $Ec$ , and  $N_r$  are shown in Figs. 21, 22, 23, 24, 25. According to plots, increasing values of all these parameters resulted in enhancing temperature and entropy variations. The higher temperature can be obtained with the augmentation of  $Bi$ ,  $Q$ , and  $N_r$ . Parameter  $Bi$  upsurge the thermal boundary layer thickness by inducing the convective heat exchange on the exterior. Meanwhile, the higher heat energy supply is contributed by  $Q$  and  $N_r$ , causing the enhancement in the temperature. Physically, higher  $N_r$  values have a more substantial influence on conduction. The radiation causes a sizable amount of heat to be emitted into the stream, which raises the temperature.  $Ec$  helps to raise the temperature while improving thermal conductance in liquid movement. The heat produced by viscous dissipation outweighs the heat being

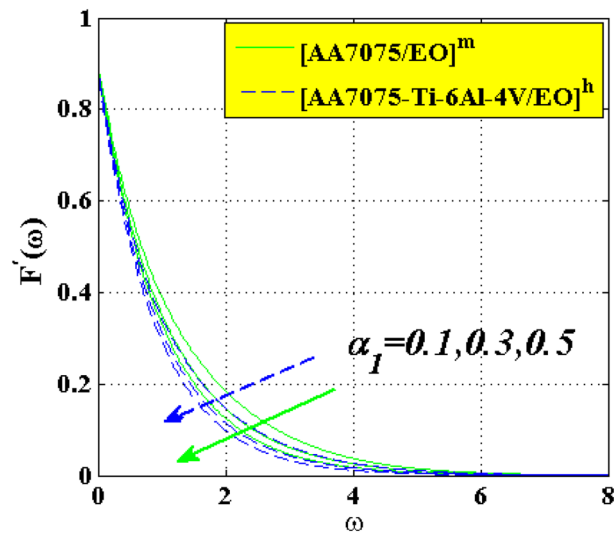


**Figure 6.** Graph of velocity with increasing  $\alpha_1$ .

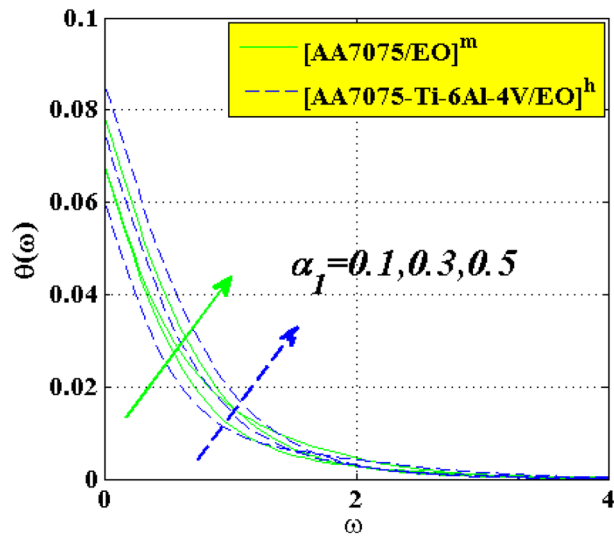


**Figure 7.** Graph of temperature with increasing  $\alpha_1$ .

transferred, resulting in thermal buildup inside the channel. The viscous dissipation increases the convection current near the pipeline, which influences the fluid temperature.

The graphical results of the suction parameter can be seen in Figs. 26, 27, 28 (velocity, temperature, and entropy). Besides, Figs. 29, 30, 31 display the injection parameter for the same profiles ( $F'(\omega)$ ,  $\theta(\omega)$ , and  $N_G$ ). From Figs. 26, 27, it can be observed that the increasing  $S > 0$  decreases  $F'(\omega)$  and  $\theta(\omega)$ . However,  $N_G$  is increased (Fig. 28). In the event of suction, the fluid under ambient conditions is drawn near the surface, reducing the thermal boundary layer thickness. The injection parameter shows an opposite effect on  $F'(\omega)$  (Fig. 29),  $\theta(\omega)$  (Fig. 30), and  $N_G$  (Fig. 31), compared to the suction parameter. Impact of  $S < 0$  (Fig. 29) is described in the following way, the injection produces a pushing force that acts on the fluid directed far from the plate, and buoyancy forces induce the fluid acceleration with minimum dependence on viscosity. Consequently, velocity is increased due to injection (Fig. 29). The same principle is applicable for suction in the opposite way as fluid is decelerated (Fig. 26). But the higher rate in the temperature profile is shown by increasing  $S < 0$  (Fig. 30). This happens as fluid is moved far from the plate, acted by the pushing force. Meanwhile, the declination of the thermal boundary layer is observed for increasing  $S > 0$  (Fig. 27).

The Reynolds number is a dimensionless number for the fluid, defined as a ratio of inertial and viscous forces. It affects the fluid flowing pattern for streamlining or laminar, steady flowing, medium-level, unstable flow (turbulent). Viscous forces serve as a resistor even though inertial forces are the most important factor in a fluid motion. Hence, fluid exhibits turbulent flowing when inertial force has the greatest impact ( $Re > 1$ ). When viscous forces become a distinguishing factor of inertial troops in the pattern of fluid flow, then the laminar flow

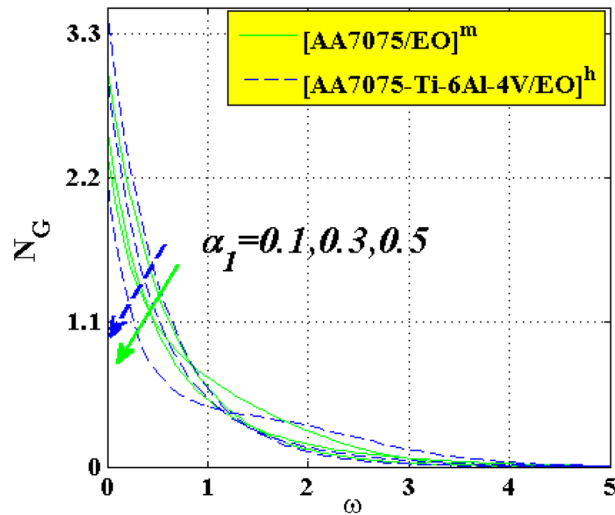


Figure 8. Graph of entropy with increasing  $\alpha_1$ .

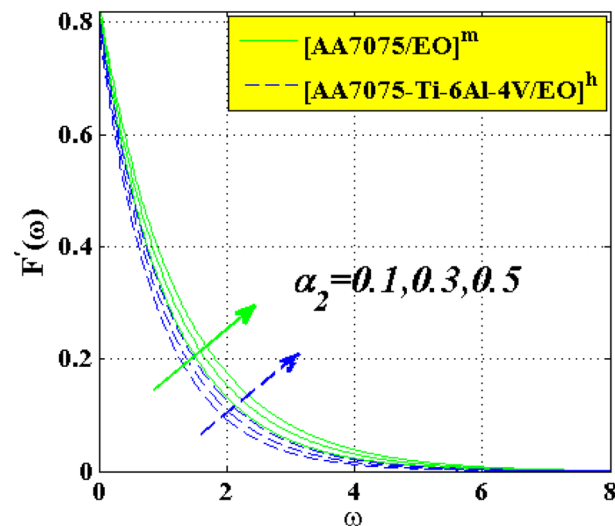


Figure 9. Graph of velocity with increasing  $\alpha_2$ .

is generated. The value of  $R_e$  this paper shows the case of turbulent flow. Figure 32 depicts the entropy profile  $N_G$  against  $R_e$ , where  $R_e$  causes the entropy to increase. Increment in  $R_e$  induces the frictional force in fluid motion, and heat is transferred in the boundary layer fluid. Therefore, entropy enhances whenever  $R_e$  increases.

The ratio of thermal dissipative to molecule thermal transference is known as the Brinkman quantity. Because heat is generated via viscous dissipative inside the liquid, the liquid's temperature will rise. However, this heat must be higher than the heat that the fluid movement causes to be lost. Entropy is another byproduct of the generation of heat. Figure 33 shows  $Br$  caused enhancement in the entropy profile of moving liquid. The explanation for this is straightforward: The Brinkman number rolled as a heat source in a fluid flow, and heat is created inside the layers of fluid particles. When the heat is transferred from the heated wall, the heat is created, and entropy is produced inside the flow channel. As a result, the Brinkman number must be kept under control to decrease entropy.

Figure 34 represents the three-dimensional bar chart of heat transmission rates for diverse  $\phi$ . Yellow colour represents nano-fluid (AA7075–EO), whereas green indicates hybrid nano-fluid (AA7075–Ti–6Al–4 V/EO). According to a bar chart, hybrid nano-fluid (AA7075–Ti–6Al–4 V/EO) gains a higher heat transport rate than nano-fluid (AA7075–EO).

The values of the Nusselt number  $N_u Re_x^{-1/2}$  are indicated in Table 4, with increasing  $\beta_1, \beta_2, \phi/\phi_h, S, Q, N_r, Bi, Ec, \gamma^*$  and  $K$ . Heat transfer is induced in the fluid flow due to all of these parameters. Additionally, with at least 22.44% and 35.01% magnitude, the thermal efficiency of AA7075–Ti–6Al–4 V/EO is higher than AA7075–EO.

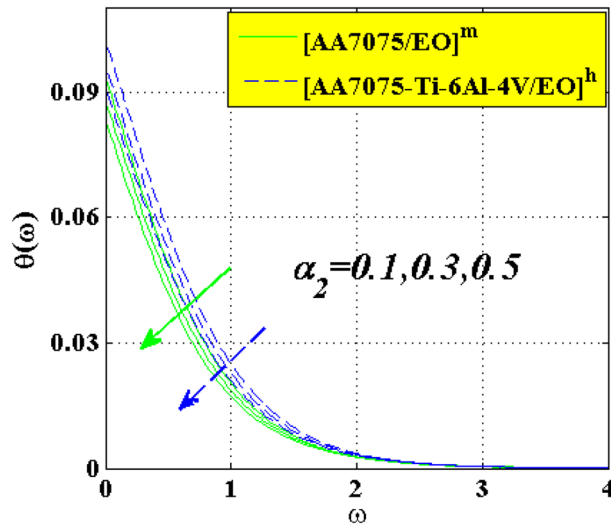


Figure 10. Graph of temperature with increasing  $\alpha_2$ .

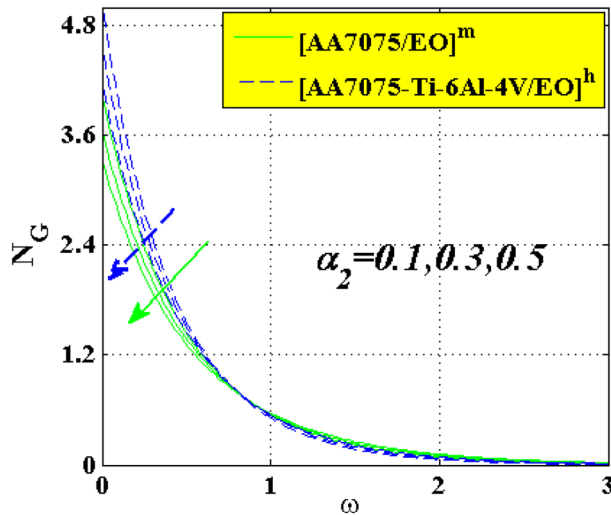


Figure 11. Graph of entropy with increasing  $\alpha_2$ .

### Final outcomes

In this paper, the numerical model of the solar water pump (SWP) has been developed, where the principal component in SWP is a parabolic trough surface collector (PTSC). The Oldroyd-B fluid in this model consists of mono nano-fluid (AA7075–EO) and hybrid nano-fluid (AA7075–Ti–6Al–4 V/EO). The controlling factors that are involved in this model are the Biot number, Brinkman number, Deborah number, Reynolds number, heat source, nanoparticle volume fraction, perforated media, radiation parameter, speed slip, viscous dissipation, suction, and injection. Changes in speed, temperature, entropy, concentration, and temperature are depicted, together with the tabulation of the Nusselt number. Therefore, the conclusion is listed below:

Speed differences tend to be due to improvements in  $\beta_2$  and  $S < 0$ .

Increases in  $\beta_1, K, \phi, \gamma^*, Bi, Q, Ec, N_r,$  and  $S < 0$  increase temperature differences.  
 The development of entropy diversity is affected by  $K, \phi, Bi, Q, Ec, N_r, S > 0, Re,$  and  $B_r$ .  
 The heat transfer rate is improved under the range of  $\beta_1, \beta_2, \phi/\phi_h, S, Q, N_r, Bi, Ec, \gamma^*$ .  
 Furthermore, at least 22.56% and a maximum of 35.01%, AA7075–Ti–6Al–4 V/EO temperature efficiency is higher than AA7075–EO.

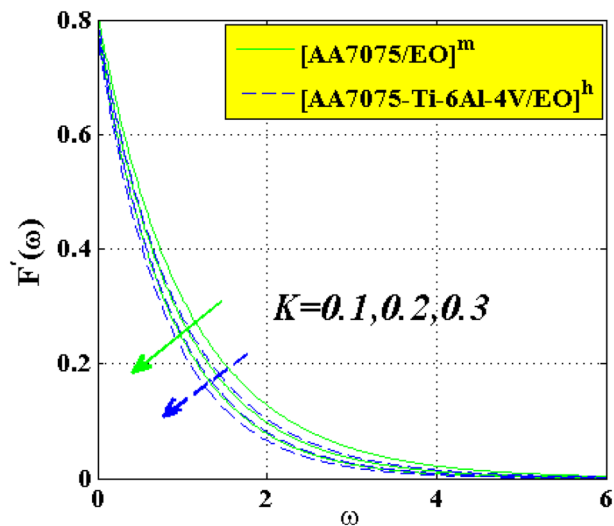


Figure 12. Graph of velocity with increasing  $K$ .

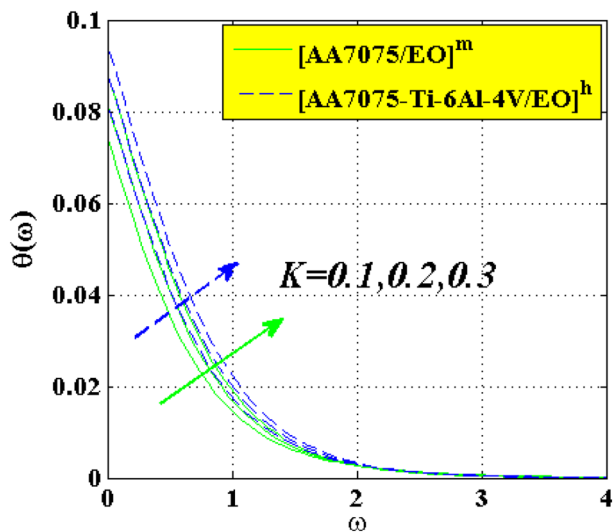


Figure 13. Graph of temperature with increasing  $K$ .

Future study recommendations include the addition of regulating variables in this current model, replacing existing factors with the right ones, and using new working fluid in PTSC.

The KBM approach could be applied to a variety of physical and technical challenges in the future<sup>81–87</sup>.

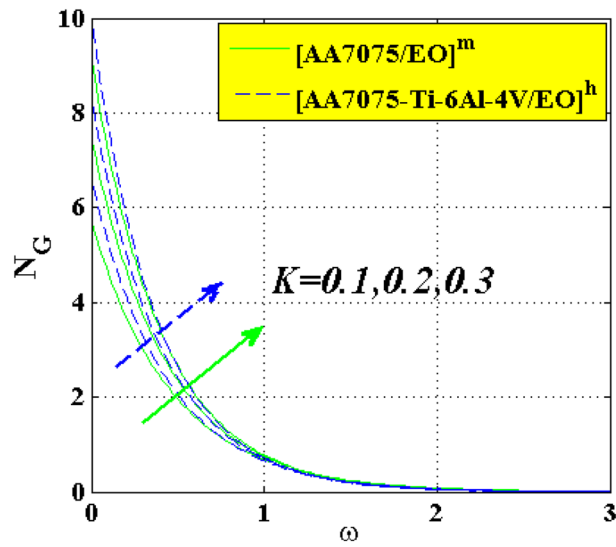


Figure 14. Graph of entropy with increasing  $K$ .

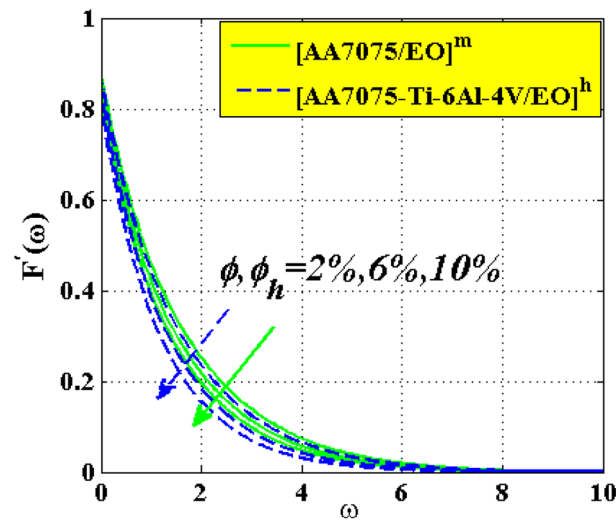


Figure 15. Graph of velocity with increasing  $\phi$ .

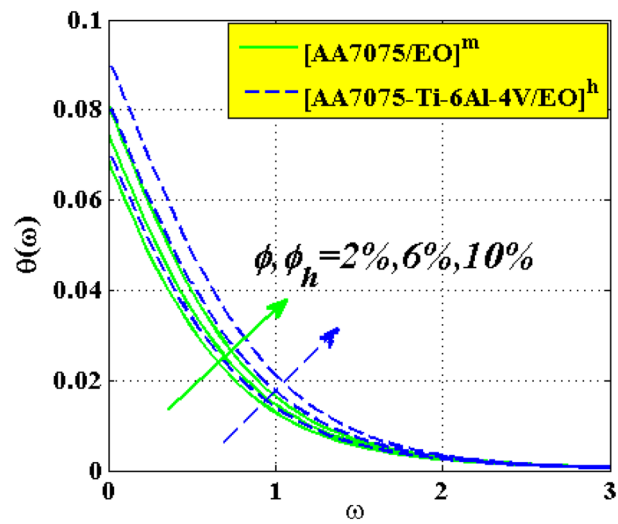


Figure 16. Graph of temperature with increasing  $\phi$ .

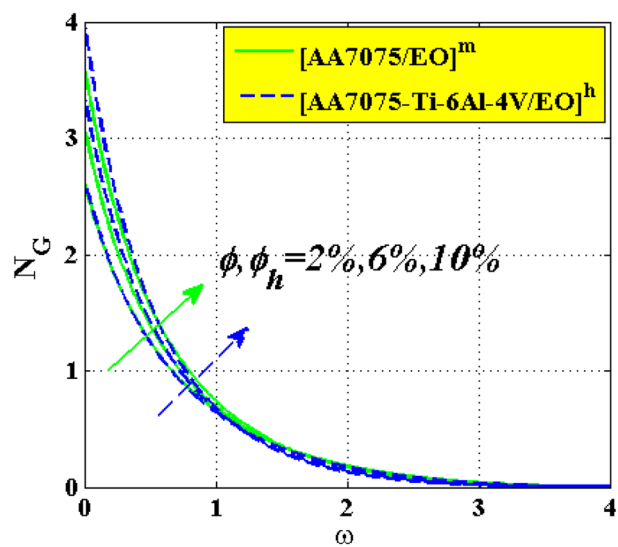


Figure 17. Graph of entropy with increasing  $\phi$ .



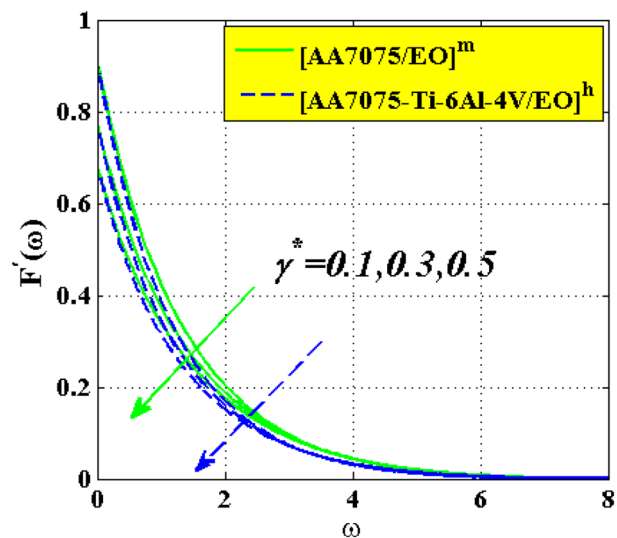


Figure 18. Graph of velocity with increasing  $\gamma^*$ .

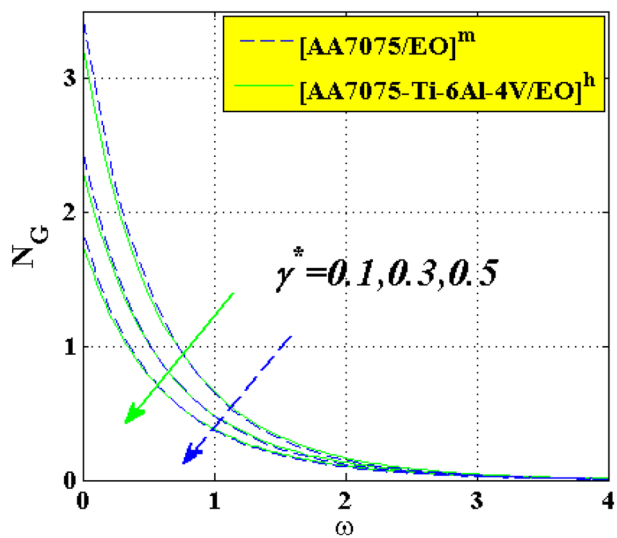


Figure 19. Graph of entropy with increasing  $\gamma^*$ .

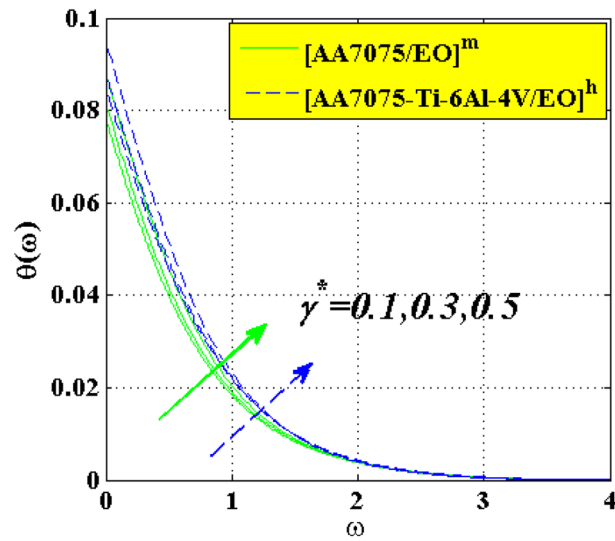


Figure 20. Graph of temperature with increasing  $\gamma^*$ .

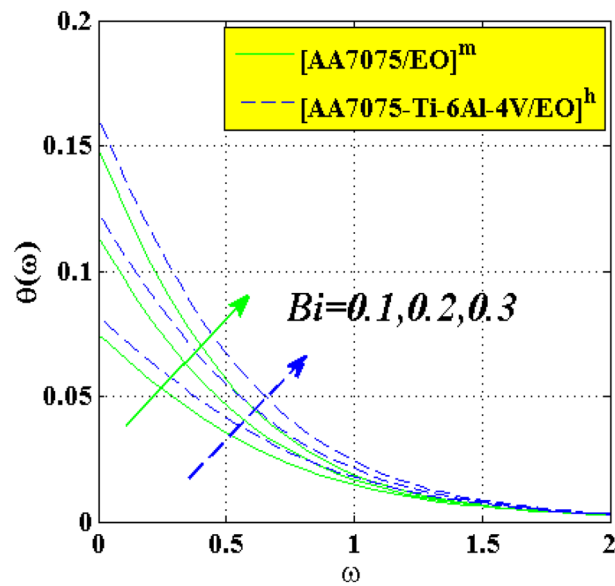


Figure 21. Graph of temperature with increasing  $Bi$ .

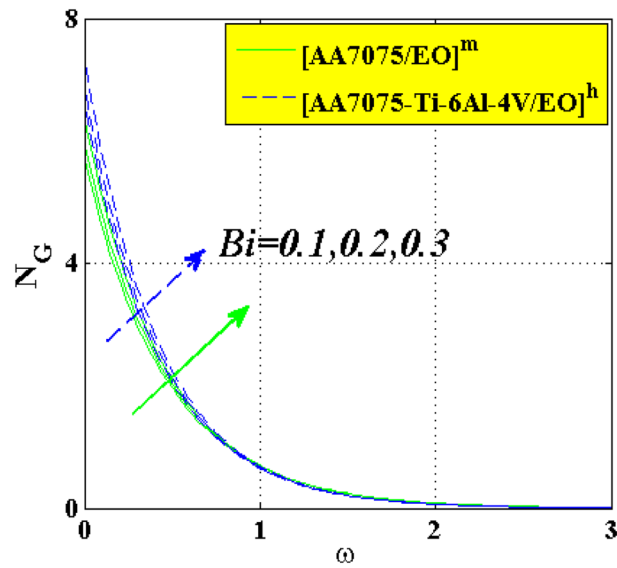


Figure 22. Graph of entropy with increasing  $Bi$ .

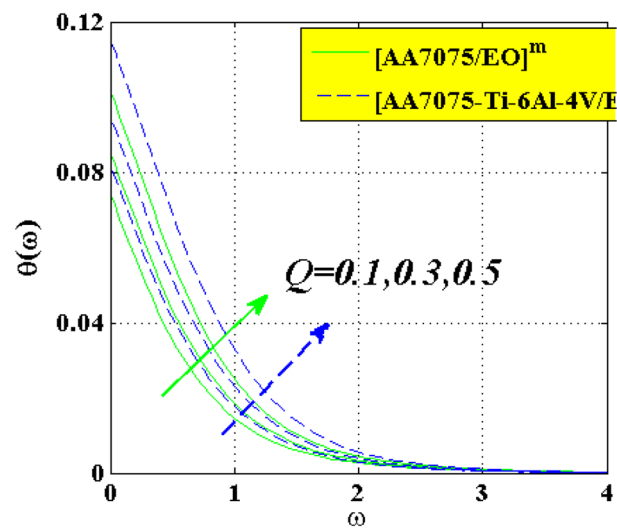


Figure 23. Graph of temperature with increasing  $Q$ .

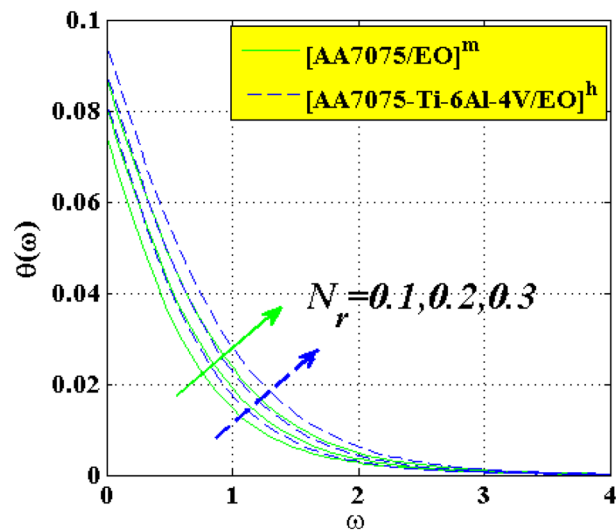


Figure 24. Graph of entropy with increasing  $N_r$ .

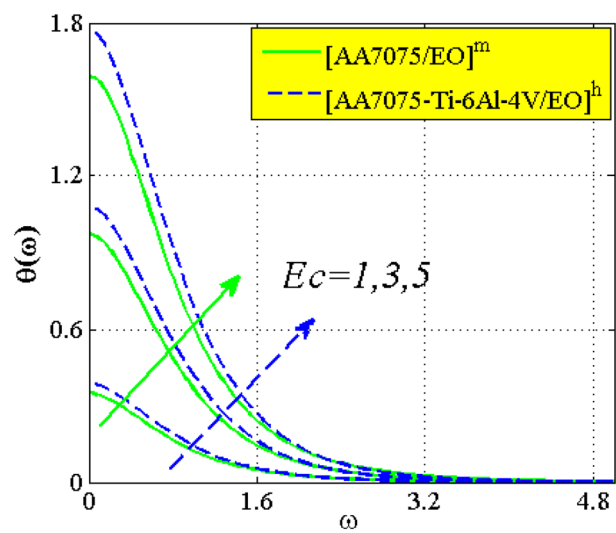


Figure 25. Graph of entropy with increasing  $E_c$ .

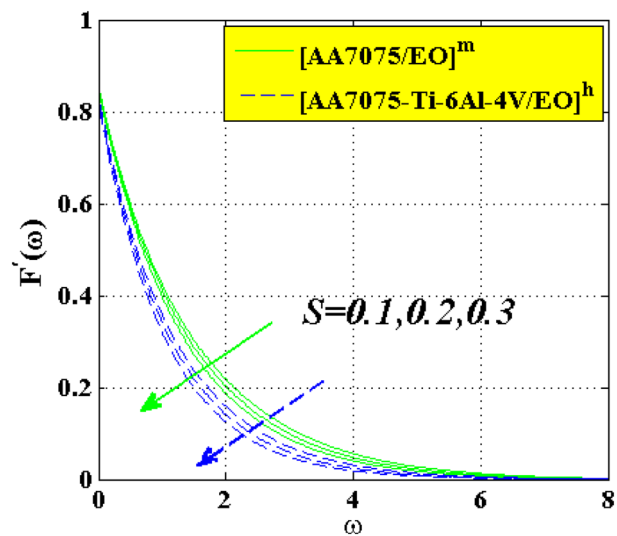


Figure 26. Graph of velocity with increasing  $S > 0$ .

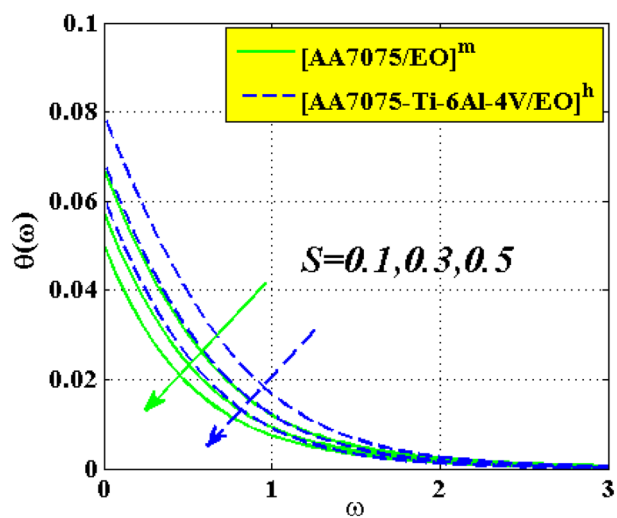


Figure 27. Graph of temperature with increasing  $S > 0$ .

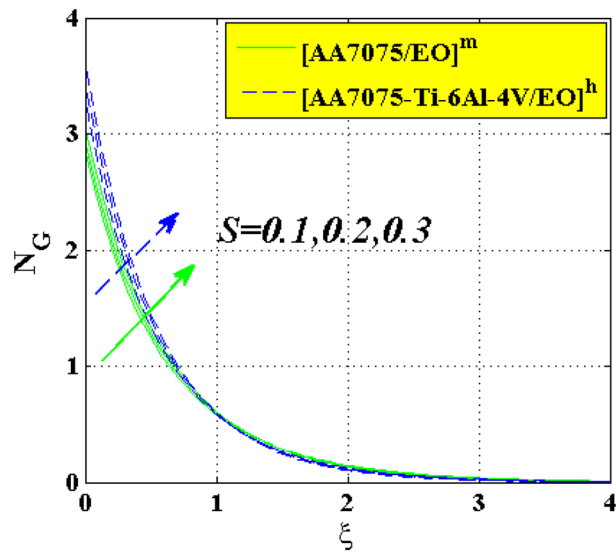


Figure 28. Graph of entropy with increasing  $S > 0$ .

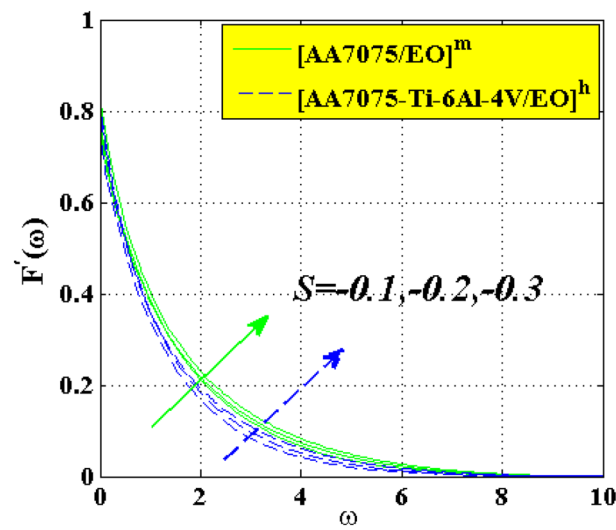


Figure 29. Graph of velocity with increasing  $S < 0$ .

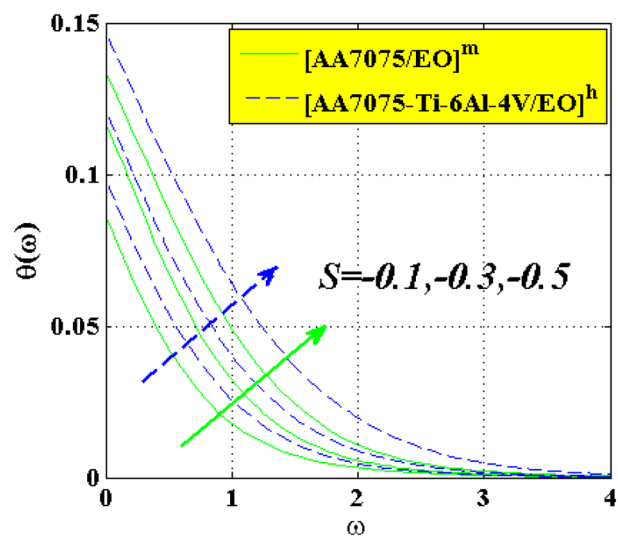


Figure 30. Graph of temperature with increasing  $S < 0$ .

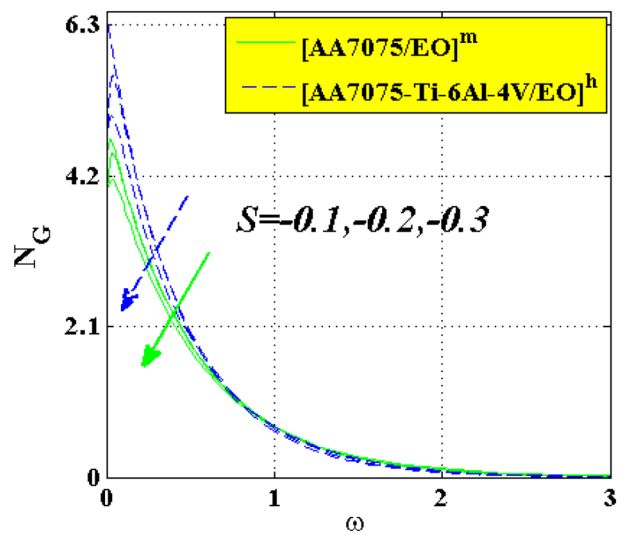


Figure 31. Graph of entropy with increasing  $S < 0$ .

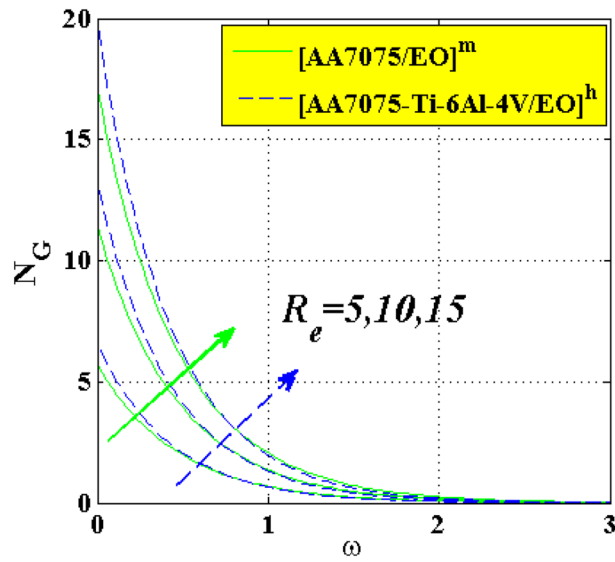


Figure 32. Graph of entropy with increasing  $Re$ .

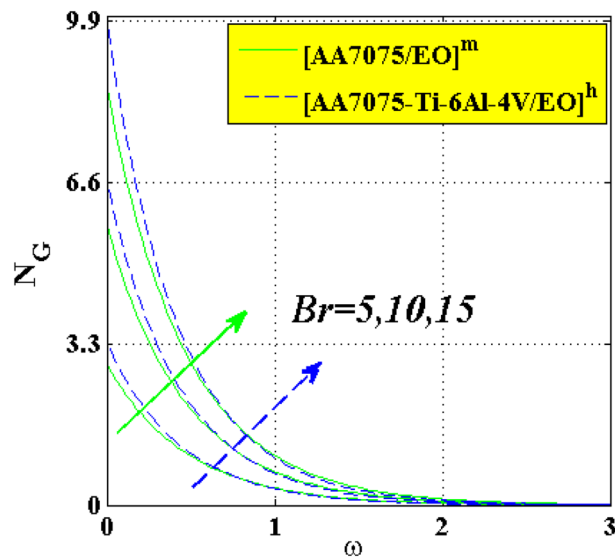


Figure 33. Graph of entropy with increasing  $Br$ .

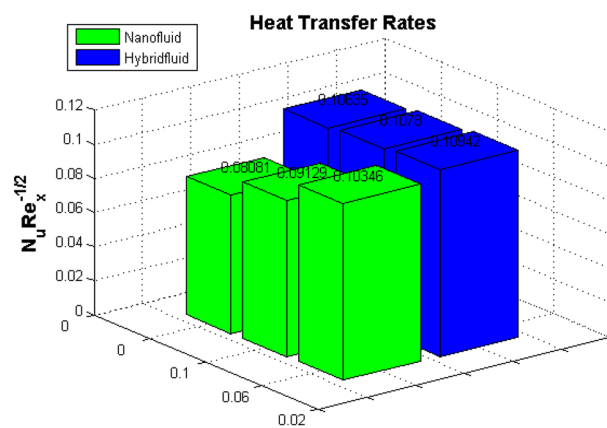


Figure 34. Impact of  $\phi$  on  $Nu Re_x^{-\frac{1}{2}}$  for mono and hybrid fluids.



## Data availability

The results of this study are available only within the paper to support the data.

Received: 23 May 2022; Accepted: 14 November 2022

Published online: 17 November 2022

## References

- Kannan, N. & Vakeesan, D. Solar energy of the coming world: -Review. *Renew. Sustain. Energy Rev.* **62**, 1092–1105 (2016).
- Fu, R., Feldman, D. J. and Margolis, R. M. US solar photovoltaic system cost benchmark: Q1 2018 (No. NREL/TP-6A20-72399). National Renewable Energy Lab. (NREL), Golden, CO (United States) (2018).
- International Energy Agency. Archived from the original (PDF) on 13 January 2012 (2011).
- Zarza, E., Rojas, M. E., Gonzalez, L., Caballero, J. M. & Rueda, F. INDITEP: DSG's first pre-commercial solar power plant. *Solar power* **80**(10), 1270–1276 (2006).
- Chan, H. Y., Riffat, S. B. & Zhu, J. A review of solar thermal and cooling technology. *Renew. Sustain. Energy Rev.* **14**(2), 781–789 (2010).
- Schulze, T. F. & Schmidt, T. W. Photochemical transformation: The current state and prospects for its use in converting solar energy. *Energy Nat. Sci.* **8**(1), 103–125 (2015).
- Bahnemann, D. Photocatalytic water treatment: Solar energy applications. *Sol. Energy* **77**(5), 445–459 (2004).
- Meinel, A. B. & Meinel, M. P. Applied solar energy: An introduction. *NASA STI/Recon Tech. Rep. A 77*, 33445 (1977).
- Ohunakin, O. S., Adaramola, M. S., Oyewola, O. M. & Fagbenle, R. O. Solar energy applications and development in Nigeria: Drivers and barriers. *Renew. Sustain. Energy Rev.* **32**, 294–301 (2014).
- Reddy, R. G. Molten salts: Thermal energy storage and heat transfer media (2011).
- Nshimyumuremyi, E. Solar water pumping system in isolated area to electricity: The case of Mibirizi village (Rwanda). *Smart Grid Renew. Energy* **6**(02), 27 (2015).
- Copeland, A. Solar water pumps in Zambia: Irrigating the Fields of Shamiyoyo (2018).
- R. Barlow, R. Mantoura, M. Gough, T. Fileman, Pigment signatures of the phytoplankton composition in the northeastern Atlantic during the 1990 spring bloom, Deep Sea Research Part II: Topical Studies in Oceanography **40** (1993) 459–477. Jan Ingenhousz, 1785.
- Fritts, C. E. On the Fritts selenium cells and batteries. *J. Franklin Inst.* **119**(3), 221–232 (1885).
- Khan, S. I., Sarkar, M. M. R. & Islam, M. Q. Design and analysis of a low cost solar water pump for irrigation in Bangladesh. *J. Mech. Eng.* **43**(2), 98–102 (2013).
- Kalogirou, S. A., Lloyd, S., Ward, J. & Eleftheriou, P. Design and performance characteristics of a parabolic-trough solar-collector system. *Appl. Energy* **47**(4), 341–354 (1994).
- Jamshed, W. *et al.* Thermal growth in solar water pump using Prandtl-Eyring hybrid nano-fluid: A solar energy application. *Sci. Rep.* **11**(1), 1–21 (2021).
- Hachicha, A. A., Rodríguez, I., Capdevila, R. & Oliva, A. Heat transfer analysis and numerical simulation of a parabolic trough solar collector. *Appl. Energy* **111**, 581–592 (2013).
- Fernández-García, A., Zarza, E., Valenzuela, L. & Pérez, M. Parabolic-trough solar collectors and their applications. *Renew. Sustain. Energy Rev.* **14**(7), 1695–1721 (2010).
- Brooks, M. J. *Performance of a parabolic trough solar collector* (Doctoral dissertation, Stellenbosch: University of Stellenbosch, 2005).
- Irfan, M., Khan, M., Khan, W. A. & Sajid, M. Thermal and solutal stratifications in flow of Oldroyd-B nano-fluid with variable conductivity. *Appl. Phys. A* **124**(10), 1–11 (2018).
- Elhanafy, A., Guaily, A. & Elsaied, A. Numerical simulation of Oldroyd-B fluid with application to hemodynamics. *Adv. Mech. Eng.* **11**(5), 1687814019852844 (2019).
- Viezel, C., Tomé, M. F., Pinho, F. T. & McKee, S. An Oldroyd-B solver for vanishingly small values of the viscosity ratio: Application to unsteady free surface flows. *J. Nonnewton. Fluid Mech.* **285**, 104338 (2020).
- Lions, P. L. & Masmoudi, N. Global solutions for some Oldroyd models of non-Newtonian flows. *Chin. Ann. Math.* **21**(02), 131–146 (2000).
- Khan, M., Ali, S. H. & Qi, H. Some accelerated flows for a generalised Oldroyd-B fluid. *Non-linear Anal.: Real World Appl.* **10**(2), 980–991 (2009).
- Nayak, M. K. *et al.* Thermo-fluidic significance of non Newtonian fluid with hybrid nanostructures. *Case Stud. Thermal Eng.* **26**, 101092 (2021).
- Sheikholeslami, M. Numerical analysis of solar energy storage within a double pipe utilising nanoparticles for expedition of melting. *Sol. Energy Mater. Sol. Cells* **245**, 111856 (2022).
- Said, Z., Sharma, P., Sundar, L. S. & Tran, V. D. Using Bayesian optimisation and ensemble boosted regression trees for optimising thermal performance of solar flat plate collector under thermosyphon condition employing MWCNT-Fe<sub>3</sub>O<sub>4</sub>/water hybrid nano-fluids. *Sustain. Energy Technol. Assess.* **53**, 102708 (2022).
- Alshukri, M. J., Hussein, A. K., Eidan, A. A. & Alsabery, A. I. A review on applications and techniques of improving the performance of heat pipe-solar collector systems. *Sol. Energy* **236**, 417–433 (2022).
- Sharma, P. *et al.* Recent advances in machine learning research for nanofluid-based heat transfer in renewable energy system. *Energy Fuels* **36**(13), 6626–6658 (2022).
- Ese, M. H., Esfandeh, S., Kamyab, M. H. & Toghraie, D. Analysis of rheological behavior of MWCNT-Al<sub>2</sub>O<sub>3</sub> (10: 90)/5W50 hybrid non-Newtonian nano-fluid with considering viscosity as a three-variable function. *J. Mol. Liq.* **341**, 117375 (2021).
- Rana, P., Srikantha, N., Muhammad, T. & Gupta, G. Computational study of three-dimensional flow and heat transfer of 25 nm Cu–H<sub>2</sub>O nanoliquid with convective thermal condition and radiative heat flux using modified Buongiorno model. *Case Stud. Thermal Eng.* **27**, 101340 (2021).
- Puneeth, V., Manjunatha, S., Madhukesh, J. K. & Ramesh, G. K. Three dimensional mixed convection flow of hybrid Casson nano-fluid past a non-linear stretching surface: A modified Buongiorno's model aspects. *Chaos, Solitons Fractals* **152**, 111428 (2021).
- Rawat, S. K., Upreti, H. and Kumar, M. Comparative study of mixed convective MHD Cu-water nano-fluid flow over a cone and wedge using modified Buongiorno's model in presence of thermal radiation and chemical reaction via Cattaneo-Christov double diffusion model. *J. Appl. Comput. Mech.* (2020)
- Rana, P., Shukla, N., Bég, O. A. & Bhardwaj, A. Lie group analysis of nano-fluid slip flow with stefan blowing effect via modified Buongiorno's model: Entropy generation analysis. *Differ. Equat. Dynam. Syst.* **29**(1), 193–210 (2021).
- Ali, B., Hussain, S., Shafique, M., Habib, D. & Rasool, G. Analysing the interaction of hybrid base liquid C<sub>2</sub>H<sub>6</sub>O<sub>2</sub>–H<sub>2</sub>O with hybrid nano-material Ag–MoS<sub>2</sub> for unsteady rotational flow referred to an elongated surface using modified Buongiorno's model: FEM simulation. *Math. Comput. Simul.* **190**, 57–74 (2021).
- Malvandi, A., Moshizi, S. A., Soltani, E. G. & Ganji, D. D. Modified Buongiorno's model for fully developed mixed convection flow of nano-fluids in a vertical annular pipe. *Comput. Fluids* **89**, 124–132 (2014).

38. J. INGENHOUSZ, Description d'une lampe a air inflammable, Nouvelles experiences et observations sur divers objets dela physique 1 (1785) 136–149.
39. R. Brown, Poseidón: a link between Semite, Hamite, and Aryan, Longmans, Green, and Company, London 1872.
40. Garg, V. K. & Jayaraj, S. Thermophoretic deposition in crossflow over a cylinder. *J. Thermophys. Heat Transfer* **4**(1), 115–116 (1990).
41. Dicke, R.H. The measurement of thermal radiation at microwave frequencies. In *Classics in Radio Astronomy* (pp. 106–113). (Springer, Dordrecht, 1946).
42. Dombrowsky, L. A. & Baillis, D. *Thermal radiation in disperse systems: An engineering approach* 35–45 (Begell House, 2010).
43. Howell, J. R., Mengüç, M. P., Daun, K. & Siegel, R. *Thermal radiation heat transfer* (CRC Press, 2020).
44. Xuan, Y. An overview of micro/nanoscaled thermal radiation and its applications. *Photon. Nanostruct.-Fundam. Appl.* **12**(2), 93–113 (2014).
45. Minea, A. A. Hybrid nano-fluids based on Al<sub>2</sub>O<sub>3</sub>, TiO<sub>2</sub> and SiO<sub>2</sub>: Numerical evaluation of different approaches. *Int. J. Heat Mass Transf.* **104**, 852–860 (2017).
46. Afrand, M., Toghray, D. & Ruhani, B. Effects of temperature and nanoparticles concentration on rheological behavior of Fe<sub>3</sub>O<sub>4</sub>-Ag/EG hybrid nano-fluid: An experimental study. *Exp. Thermal Fluid Sci.* **77**, 38–44 (2016).
47. Awan, A. U., Safdar, R., Shaukat, A. and Shaukat, A. Effects of chemical reaction on the unsteady flow of an incompressible fluid over a vertical oscillating plate. *Punjab Univ. J. Math.*, **48**(2) (2020).
48. Hynes, J. T. Chemical reaction dynamics in solution. *Annu. Rev. Phys. Chem.* **36**(1), 573–597 (1985).
49. Chambré, P. L. & Young, J. D. On the diffusion of a chemically reactive species in a laminar boundary layer flow. *Phys. Fluids* **1**(1), 48–54 (1958).
50. Ramanamurthy, K. V. and Govinda Rao, V. M. H. Incompressible laminar boundary layer flow around a cylindrical catalyst pellet with first order chemical reaction. In *Proc. of First National HMT conference* (pp. 1–8) (1971).
51. Nadeem, S., Hayat, T. & Khan, A. U. Numerical study of 3D rotating hybrid SWCNT-MWCNT flow over a convectively heated stretching surface with heat generation/absorption. *Phys. Scr.* **94**(7), 075202 (2019).
52. Yusuf, T. A., Mabood, F., Khan, W. A. & Gbadeyan, J. A. Irreversibility analysis of Cu-TiO<sub>2</sub>-H<sub>2</sub>O hybrid-nanofluid impinging on a 3-D stretching sheet in a porous medium with non-linear radiation: Darcy-Forchheimer's model. *Alex. Eng. J.* **59**(6), 5247–5261 (2020).
53. Mabood, F., Yusuf, T. A., Rashad, A. M., Khan, W. A. & Nabwey, H. A. Effects of combined heat and mass transfer on entropy generation due to MHD nano-fluid flow over a rotating frame. *CMC-Comput. Mater. Continua* **66**(1), 575–587 (2021).
54. Aziz, A., Jamshed, W., Ali, Y. & Shams, M. Heat transfer and entropy analysis of Maxwell hybrid nano-fluid including effects of inclined magnetic field, Joule heating and thermal radiation. *Discrete Contin. Dyn. Syst.-S* **13**(10), 2667 (2020).
55. Mabood, F., Yusuf, T. A. & Bognár, G. Features of entropy optimisation on MHD couple stress nano-fluid slip flow with melting heat transfer and non-linear thermal radiation. *Sci. Rep.* **10**(1), 1–13 (2020).
56. Mabood, F., Yusuf, T. A. & Khan, W. A. Cu-Al<sub>2</sub>O<sub>3</sub>-H<sub>2</sub>O hybrid nano-fluid flow with melting heat transfer, irreversibility analysis and non-linear thermal radiation. *J. Therm. Anal. Calorim.* **143**(2), 973–984 (2021).
57. Cheng, W. T. & Lin, C. H. Transient mixed convective heat transfer with melting effect from the vertical plate in a liquid saturated porous medium. *Int. J. Eng. Sci.* **44**(15–16), 1023–1036 (2006).
58. Kairi, R. R. and Murthy, P. V. S. N. Effect of melting on mixed convection heat and mass transfer in a non-Newtonian fluid saturated non-Darcy porous medium. *J. Heat Transf.*, **134**(4) (2012).
59. Bein, B. Entropy. *Best Pract. Res. Clin. Anaesthesiol.* **20**(1), 101–109 (2006).
60. Gray, R.M., 2011. *Entropy and information theory*. Springer Science & Business Media.
61. Sciacovelli, A., Verda, V. & Sciubba, E. Entropy generation analysis as a design tool—a review. *Renew. Sustain. Energy Rev.* **43**, 1167–1181 (2015).
62. ManjuAnath, K. & Kaushik, S. C. Second law thermodynamic study of heat exchangers: A review. *Renew. Sustain. Energy Rev.* **40**, 348–374 (2014).
63. Torabi, M., Karimi, N., Peterson, G. P. & Yee, S. Challenges and progress on the modelling of entropy generation in porous media: A review. *Int. J. Heat Mass Transf.* **114**, 31–46 (2017).
64. Mahian, O. *et al.* A review of entropy generation in nano-fluid flow. *Int. J. Heat Mass Transf.* **65**, 514–532 (2013).
65. Sen, S. S. S., Das, M., Mahato, R. & Shaw, S. Entropy analysis on non-linear radiative MHD flow of diamond-Co<sub>3</sub>O<sub>4</sub>/ethylene glycol hybrid nano-fluid with catalytic effects. *Int. Commun. Heat Mass Transf.* **129**, 105704 (2021).
66. Shahzad, F. *et al.* Comparative numerical study of thermal features analysis between oldroyd-B copper and molybdenum disulfide nanoparticles in engine-oil-based nanofluids flow. *Coatings* **11**(10), 1196 (2021).
67. Aziz, A., Jamshed, W. & Aziz, T. Mathematical model for thermal and entropy analysis of thermal solar collectors by using Maxwell nano-fluids with slip conditions, thermal radiation and variable thermal conductivity. *Open Phys.* **16**, 123–136 (2018).
68. Jamshed, W. Numerical investigation of MHD Impact on maxwell nanofluid. *Int. Commun. Heat Mass Transf.* **120**, 104973 (2021).
69. Jamshed, W. Thermal augmentation in solar aircraft using tangent hyperbolic hybrid nano-fluid: A solar energy application, *Energy Environ.* 1–44 (2021).
70. Jamshed, W., Devi S, S. U., Safdar, R., Redouane, F., Nisar. K. S., and Eid, M. R., Comprehensive analysis on copper-iron (II, III)/oxide-engine oil Casson nano-fluid flowing and thermal features in parabolic trough solar collector, *J. Taibah Univ. Sci.*, **15**(1), 619–636.
71. Hou, C., Yang, G., Yang, W. & Chen, J. Study of thermo-fluidic characteristics for geometric-anisotropy Kagome truss-cored lattice. *Chin. J. Aeronaut.* **32**(7), 1635–1645 (2019).
72. Brewster, M. Q. *Thermal radiative transfer and features* (John Wiley and Sons, 1992).
73. Hussain, S. M. & Jamshed, W. A comparative entropy based analysis of tangent hyperbolic hybrid nano-fluid flow: Implementing finite difference method. *Int. Commun. Heat Mass Transf.* **129**, 105671 (2021).
74. Jamshed, W., Mohd Nasir, N. A. A., Mohamed Isa, S. S. P., Safdar, R., Shahzad, F., Nisar, K.S., Eid, M. R., Abdel-Aty, A. H. and Yahia, I. S. Thermal growth in solar water pump using Prandtl-Eyring hybrid nano-fluid: a solar energy application, *Scientific Reports* (2021).
75. Keller, H. B. A new difference scheme for parabolic problems, *Hubbard, B., Ed., numerical solutions of partial differential equations*, **2**, 327–350 (1971).
76. Ishak, A., Nazar, R. & Pop, I. Mixed convection on the stagnation point flow towards a vertical, continuously stretching sheet. *J. Heat Transfer-ASME* **129**, 1087–1090 (2007).
77. Ishak, A., Nazar, R. & Pop, I. Boundary layer flow and heat transfer over an unsteady stretching vertical surface. *Meccanica* **44**, 369–375 (2007).
78. Abolbashari, M. H., Freidoonimehr, N., Nazari, F. & Rashidi, M. M. Entropy analysis for an unsteady MHD flow past a stretching permeable surface in nano-fluid. *Powder Technol.* **267**, 256–267 (2014).
79. Das, S., Chakraborty, S., Jana, R. N. & Makinde, O. D. Entropy analysis of unsteady magneto-nanofluid flow past accelerating stretching sheet with convective boundary condition. *Appl. Math. Mech.* **36**(2), 1593–1610 (2015).
80. Jamshed, W. & Nisar, K. S. Computational single phase comparative study of Williamson nanofluid in parabolic trough solar collector via keller box method. *Int. J. Energy Res.* **45**(7), 10696–10718 (2021).
81. Pasha, A. A. *et al.* Statistical analysis of viscous hybridized nanofluid flowing via Galerkin finite element technique. *Int. Commun. Heat Mass Transfer* **137**, 106244 (2022).

82. Hussain, S. M., Jamshed, W., Pasha, A. A., Adil, M. & Akram, M. Galerkin finite element solution for electromagnetic radiative impact on viscid Williamson two-phase nanofluid flow via extendable surface. *Int. Commun. Heat Mass Transfer* **137**, 106243 (2022).
83. Hafeez, M. B., Krawczuk, M., Nisar, K. S., Jamshed, W. & Pasha, A. A. A finite element analysis of thermal energy inclination based on ternary hybrid nanoparticles influenced by induced magnetic field. *Int. Commun. Heat Mass Transfer* **135**, 106074 (2022).
84. Jamshed, W. *et al.* Physical specifications of MHD mixed convective of Ostwald-de Waele nanofluids in a vented-cavity with inner elliptic cylinder. *Int. Commun. Heat Mass Transfer* **134**, 106038 (2022).
85. Shah, N. A., Wakif, A., El-Zahar, E. R., Ahmad, S. & Yook, S. J. Numerical simulation of a thermally enhanced EMHD flow of a heterogeneous micropolar mixture comprising (60%)-ethylene glycol (EG), (40%)-water (W), and copper oxide nanomaterials (CuO). *Case Stud. Thermal Eng.* **35**, 102046 (2022).
86. Shah, N. A., Wakif, A., El-Zahar, E. R., Thumma, T. & Yook, S.-J. Heat transfers thermodynamic activity of a second-grade ternary nanofluid flow over a vertical plate with Atangana-Baleanu time-fractional integral. *Alex. Eng. J.* **61**(12), 10045–10053 (2022).
87. Dinesh Kumar, M., Raju, C. S. K., Sajjan, K. El-Zahar E. R. and Shah, N. A. Linear and quadratic convection on 3D flow with transpiration and hybrid nanoparticles, *Int. Commun. Heat Mass Transfer*

### Author contributions

Conceptualization: F.S. Formal analysis: M.R.E. Investigation: W.J. Methodology: R.S. & M.R.E. Software: F.S. & S.S.P.M.I. Re-Graphical representation & Adding analysis of data: S.M.E.D. Writing—original draft: M.R.E. & N.A.A.M.N. Writing—review editing: A.I. Numerical process breakdown: S.M.E.D. Re-modelling design: W.J. & A.I. Re-Validation: S.M.E.D. & W.J. Furthermore, all the authors equally contributed to the writing and proofreading of the paper. All authors reviewed the manuscript.

### Competing interests

The authors declare no competing interests.

### Additional information

**Supplementary Information** The online version contains supplementary material available at <https://doi.org/10.1038/s41598-022-24294-3>.

**Correspondence** and requests for materials should be addressed to M.R.E.

**Reprints and permissions information** is available at [www.nature.com/reprints](http://www.nature.com/reprints).

**Publisher's note** Springer Nature remains neutral with regard to jurisdictional claims in published maps and institutional affiliations.



**Open Access** This article is licensed under a Creative Commons Attribution 4.0 International License, which permits use, sharing, adaptation, distribution and reproduction in any medium or format, as long as you give appropriate credit to the original author(s) and the source, provide a link to the Creative Commons licence, and indicate if changes were made. The images or other third party material in this article are included in the article's Creative Commons licence, unless indicated otherwise in a credit line to the material. If material is not included in the article's Creative Commons licence and your intended use is not permitted by statutory regulation or exceeds the permitted use, you will need to obtain permission directly from the copyright holder. To view a copy of this licence, visit <http://creativecommons.org/licenses/by/4.0/>.

© The Author(s) 2022